A positive feedback-based mechanism for constriction rate acceleration during cytokinesis in *C. elegans*

Renat N. Khaliullin[1]*, Rebecca A. Green[1], Linda Z. Shi[2], J. Sebastian Gomez-Cavazos[1], Michael W. Berns[2], Arshad Desai[1], and Karen Oegema[1]*

[1]Department of Cellular and Molecular Medicine, Ludwig Institute for Cancer Research, University of California, San Diego, La Jolla, CA 92093, USA.

[2]Department of Bioengineering and Institute of Engineering in Medicine, University of California, San Diego, 9500 Gilman Drive, La Jolla, CA, 92093, USA

*Correspondence to: Karen Oegema (koegema@ucsd.edu); Renat N. Khaliullin (renatkh@gmail.com)

ABSTRACT

During cytokinesis, an equatorial actomyosin contractile ring constricts at a relatively constant overall rate despite its progressively decreasing size. Thus, the per-unit-length rate of ring closure increases as ring perimeter decreases. To understand this acceleration, we monitored cortical surface and ring component dynamics during the first division of the *C. elegans* embryo. We show that the polar cortex expands during ring constriction to provide the cortical surface area required for division. Polar expansion also allows ring myosin to compress cortical surface along the pole-to-pole axis, leading to a continuous flow of cortical surface into the ring. We propose that feedback between ring myosin and compression-driven cortical flow drives an exponential increase in the amount of ring myosin that maintains the high overall closure rate as ring perimeter decreases. We further show that an analytical mathematical formulation of the proposed feedback, called the Compression Feedback model, recapitulates the experimental observations.

IMPACT STATEMENT: During cytokinesis, positive feedback between myosin motors in the contractile ring and compression-driven cortical flow along the axis perpendicular to the ring drives constriction rate acceleration to ensure timely cell separation.

MAJOR SUBJECT AREAS: Cell biology, Computational and Systems Biology

KEYWORDS: contractile ring, compression feedback model, cortical surface compression, analytical mathematical model, myosin II, anillin

INTRODUCTION

During cytokinesis in animal cells, constriction of an equatorial actomyosin ring cinches the mother cell surface to generate a dumbbell-shaped structure with an intercellular bridge that connects the two daughter cells (Fededa and Gerlich, 2012; Green et al., 2012). Following chromosome segregation in anaphase, the contractile ring assembles in response to signaling by the anaphase spindle that activates RhoA at the cell equator (Green et al., 2012; Jordan and Canman, 2012; Piekny et al., 2005). RhoA patterns the equatorial cortex by recruiting contractile ring components from the cytoplasm (Vale et al., 2009; Yumura, 2001; Zhou and Wang, 2008). RhoA activates Rho kinase, which promotes the assembly and recruitment of myosin II (Matsumura et al., 2011) and the formin that assembles the long actin filaments that make up the ring (Otomo et al., 2005). Contractile rings also contain membrane-associated septin filaments (Bridges and Gladfelter, 2015) and the filament cross linker anillin (D'Avino, 2009; Piekny and Maddox, 2010). Recent work in the *C. elegans* embryo suggests that the equatorial cortex is compressed after this initial patterning, leading to the alignment of actin filament bundles as the ring forms (Reymann et al., 2016). After its assembly, the ring begins to constrict in the around-the-ring direction. Constriction is thought to be coupled to the progressive disassembly of the ring (i.e. loss of components in proportion to reduction in length) (Murrell et al., 2015; Schroeder, 1990).

Ring constriction must complete within a short cell cycle window during mitotic exit (Canman et al., 2000; Martineau et al., 1995; Straight et al., 2003). Timely constriction relies on the conserved ability of contractile rings to maintain a relatively constant overall closure rate despite their progressively decreasing perimeter (Biron et al., 2004; Bourdages et al., 2014; Calvert et al., 2011; Carvalho et al., 2009; Ma et al., 2012; Mabuchi, 1994; Pelham and Chang, 2002; Zumdieck et al., 2007). This property implies that the per-unit-length constriction rate increases as the rings get smaller. Prior work has suggested that this acceleration could arise if a constriction-rate controlling element is retained, rather than lost due to disassembly, as the ring shortens. For example, if myosin motors are not lost as the ring constricts, its concentration would increase in proportion to the reduction in perimeter, which could explain why the per-unit-length constriction rate increases as the ring shortens. Alternatively, it has been

64 proposed that the number of actin filaments could be retained. If actin filaments shorten from their ends
65 during constriction, the overall amount of actin polymer could decrease in proportion to the reduction in
66 perimeter while the number of filament ends remains constant, perhaps leading to observed increase in
67 the per-unit-length constriction rate (Carvalho et al., 2009).

68 Here, we explore the mechanisms underlying constriction rate acceleration during the first
69 division of the *C. elegans* embryo. By generating a 4D map of cortical surface dynamics, we show that
70 cortex at the cell poles expands in response to the tension generated by the constricting ring to provide
71 the increased cortical surface area required to generate the daughter cells. The ability of the polar cortex
72 to expand in response to tension also allows ring myosin to compress cortical surface along the pole-to-
73 pole axis perpendicular to the ring, leading to a continuous flow of cortical surface into the ring during
74 constriction. We show that the ring compresses cortical surface throughout cytokinesis at a rate
75 proportional to the amount of ring myosin. In addition, the amount of ring myosin increases in proportion
76 to the amount of cortical surface pulled into the ring by compression. The per-unit-length amount of ring
77 myosin and the per-unit-length rates of cortical compression and ring constriction increase with the same
78 exponential kinetics as the ring closes, suggesting control by positive feedback. Based on our
79 observations, we propose that feedback between ring myosin and compression-driven cortical flow
80 drives ring myosin accumulation, which in turn increases the per-unit-length constriction rate to keep the
81 overall constriction rate high as the ring closes. We show that an analytical mathematical formulation of
82 the proposed feedback, called the Compression Feedback model, recapitulates our experimental
83 observations.
84

RESULTS

The cortex at the cell poles expands in response to tension generated by the constricting ring without limiting the constriction rate

During the first division of the *C. elegans* embryo, the surface area of the cell increases by ~40% to accommodate the shape change that generates the daughter cells. Work in multiple systems has shown that the entire cell surface, from cortex-associated granules in the cytoplasm to cell surface receptors, moves in a coordinated fashion during cytokinesis (Cao and Wang, 1990; Dan, 1954; Dan and Dan, 1940; Dan et al., 1938; DeBiasio et al., 1996; Fishkind et al., 1996; Hird and White, 1993; Reymann et al., 2016; Swann and Mitchison, 1958; Wang et al., 1994). In a classic set of experiments, Dan and colleagues measured the distance between surface adhered particles to monitor changes in cortical surface area (compression and expansion) during cytokinesis in sea urchin embryos. This analysis revealed that ring constriction occurs coincident with a wave of cortical expansion that initiates at the cell poles and propagates towards the furrow (Dan et al., 1938; Dan and Ono, 1954; Dan et al., 1937; Swann and Mitchison, 1958). Although these experiments provided a rough map of where expansion occurs, they did not allow quantification of the extent of change in cortical surface area or provide a map of cortical surface movements. Note that the analysis of cell surface dynamics described above refers to movement, expansion and compression of the cortex and associated structures. How deposition of plasma membrane, the fluid lipid layer that overlies the cortex, is controlled and where it occurs are distinct questions that we will not discuss here.

To generate a quantitative map of cortical surface dynamics during the first division of the *C. elegans* embryo, we employed an updated version of the classical approach in which we used myosin foci rather than surface adhered particles as fiduciary marks. We imaged the cortex at high time resolution (**2s intervals**, **cyan box in Figure 1A, Video 1**) in embryos expressing a GFP fusion with the heavy chain of non-muscle myosin II (NMY-2; hereafter myosin::GFP; **Figure 1 – Figure Supplement 1A,B**). In addition to its RhoA-dependent enrichment in the contractile ring, myosin is in small puncta, distributed over the entire cortex, that flow together with actin filaments (LifeAct::mKate2, **Figure 1 – Figure Supplement 1C**), validating their utility as fiduciary marks for monitoring cortical movements. To

112 temporally and spatially align data collected in different embryos, ring constriction was also monitored at
113 lower time resolution in the same embryos (**36s intervals**, **Figure 1A, Figure 1 – Figure Supplement**
114 **2**). Because the contractile ring closes asymmetrically within the division plane ((Maddox et al., 2007);
115 **Figure 1A, Figure 1 – Figure Supplement 2**), cortical dynamics are not cylindrically symmetric.
116 Therefore, we generated an average 4D map of cortical movement by computationally combining data
117 from 93 embryos imaged in random rotational orientations (**Figure 1A, Figure 1 – Figure Supplement**
118 **2**). We defined the top of the embryo as the side where the furrow ingresses first, the bottom as the
119 opposite side, and referenced positions around the embryo circumference by the angle θ relative to the
120 initial ingression axis (**Figure 1A**). For temporal alignment, we fit a line to normalized ring size ($\bar{R} :=$
121 R/R_{emb}) versus time between 30% and 80% closure for each embryo, and extrapolated this line to 1 and
122 0 to define t_0 (cytokinesis onset) and t_{CK} (time of cytokinesis), respectively (**Figure 1A, Figure 1 – Figure**
123 **Supplement 2**). Cortical movement could not be monitored in the division plane, because it is hidden
124 inside the cell, or at the cell poles, due to their high curvature. Thus, this approach provided a
125 quantitative picture of cortical movement in the central 2/3 of the embryo throughout cytokinesis (**Figure**
126 **1B**; **Video 2**).

127 The 4D map allowed us to determine where cortical surface expansion occurs as the ring closes
128 in the *C. elegans* embryo. Prior work monitoring the movement of surface adhered particles in sea urchin
129 and *Xenopus* embryos indicated that surface expansion occurs at the poles and immediately behind the
130 contractile ring, respectively, in these systems (Bluemink and de Laat, 1973; Byers and Armstrong, 1986;
131 Danilchik et al., 2003; Gudejko et al., 2012; Selman and Perry, 1970; Swann and Mitchison, 1958). In
132 addition to these two patterns, we also considered the possibility that the cortex would expand uniformly,
133 an assumption often used in models of cytokinesis (Turlier et al., 2014; Zumdieck et al., 2007). Each of
134 these three patterns predicts a different profile for the Anterior-Posterior (AP) component of cortical
135 velocity along the embryo. For uniform surface expansion, a gradient of velocities is predicted, where the
136 cortical velocity immediately behind the ring equals the velocity of furrow ingression and the velocity
137 decreases linearly towards the cell poles. For surface expansion behind the ring, no cortical movement is
138 predicted on the observable embryo surface. If surface expansion is limited to the poles, the cortical

139 velocity is predicted to be constant within the flow map region (**Figure 1 – Figure Supplement 3**). The
140 cortical velocity profile measured from the flow map indicated that the cortical surface at the cell poles
141 expands as the ring constricts, whereas the cortex between the poles and the division plane flows at
142 constant velocity towards the division plane, without expansion or compression (**Figure 1B**). Note that
143 the apparent velocity gradient that spans the division plane (**Figure 1B**, ***dashed regions on velocity***
144 ***curves***) is a projection artifact due to the fact that the cortical surface turns inwards as it approaches the
145 furrow from either side. As expected, based on the asymmetric closure of the contractile ring within the
146 division plane, the velocity of cortical flow was higher on the top of the embryo during the first half of
147 cytokinesis when the furrow ingresses from the top (**Figure 1B, black traces**) and became higher on the
148 bottom of the embryo towards the end when the furrow ingresses from the bottom (**Figure 1B, grey**
149 **traces; Video 2**).

150 Cutting the cortex parallel to the division plane using a laser revealed that the cortex is under
151 tension during cytokinesis (**Figure 2A**). To determine if cortical tension limits the constriction rate, we
152 assayed the effect of the cortical cuts on ring closure. Cortical cuts spanning the visible area of cortex on
153 the anterior side of the embryo (~10um in length) were made parallel to the division plane when the ring
154 was at ~50% closure, and the effect on contractile ring closure rate was assessed by measuring the
155 difference in ring sizes immediately before and 13s after the cut. The cortical opening resulting from the
156 ablation was approximately 35μm^2, which would be expected to increase the constriction rate from the
157 control rate of 0.22 $\pm$ 0.5 μm/s to ~0.25 μm/s over our 13s interval if the cortical surface tension is the
158 dominant force limiting the ring closure rate (**see Methods for details**). In contrast, the measured
159 constriction rate after was not increased after cutting (0.18 $\pm$ 0.03 μm/s; **Figure 2B,C**), indicating that
160 cortical tension does not impose significant resistance to ring pulling. Cuts made perpendicular to the
161 ring also had no effect on the constriction rate (0.19 $\pm$ 0.03 μm/s **data not shown**). Consistent with the
162 results of the laser cutting experiments, inhibiting the Arp2/3 complex by depleting its ARX-2 subunit,
163 which is expected to reduce effective cortical viscosity and thus cortical tension (Chaudhuri et al., 2007;
164 Davies et al., 2014; Tseng and Wirtz, 2004), also did not alter the constriction rate (**Figure 2 – Figure**
165 **Supplement 1A**).

166 Putting the results of our flow map analysis with our laser cutting and Arp2/3 inhibition
167 experiments together, we conclude that the cortex at the poles expands in response to tension
168 generated by the constricting ring without providing significant resistance that would affect the rate of ring
169 closure. In contrast, the cortex in the region between the ring and the poles flows towards the ring
170 without expansion or compression. The differential response of the polar cortex to ring-generated tension
171 is consistent with the idea of polar relaxation hypothesized in early conceptual models of cytokinesis
172 (Greenspan, 1978; Swann and Mitchison, 1958; Taber, 1995; White and Borisy, 1983; Wolpert, 1960;
173 Zinemanas and Nir, 1987; Zinemanas and Nir, 1988), and suggests that the polar cortex has unique
174 mechanical properties compared to the intervening cortex that does not expand (see discussion for
175 possibilities). The fact that cortical tension does not limit the rate of ring constriction suggests that the
176 constriction rate is instead limited by ring internal friction. We conclude that the viscosity of the polar
177 cortex is negligible compared to the viscosity internal to the ring; thus, ring myosin generated force
178 primarily counters ring internal friction to drive ring constriction (**Figure 2 – Figure Supplement 1B**).
179 Ring constriction, in turn, affects cortical tension and drives expansion of polar cortex.
180
181 ***Ring myosin compresses cortical surface along the pole-to-pole axis perpendicular to the ring,***
182 ***pulling in new cortical surface at a rate proportional to the amount of ring myosin***
183 In the *C. elegans* embryo, as in other systems, spindle-based signaling activates RhoA on the
184 equatorial cortex following anaphase onset leading to the recruitment of contractile ring proteins
185 including myosin II, the septins, and anillin (Jenkins et al., 2006; Maddox et al., 2005; Maddox et al.,
186 2007; Mangal et al., 2018; Motegi and Sugimoto, 2006; Schonegg et al., 2007; Tse et al., 2012; Werner
187 et al., 2007). An astral microtubule based mechanism that clears contractile ring proteins from the polar
188 cortex also confines contractile ring protein recruitment to a defined equatorial zone (Mangal et al., 2018;
189 Werner et al., 2007). Prior work in the *C. elegans* embryo has suggested that the equatorial cortex is
190 compressed during contractile ring assembly, coincident with the alignment of actin filament bundles to
191 form the ring (Reymann et al., 2016). Cortical surface compression is detected as a gradient in the
192 velocity of cortical surface flow. Consistent with the idea that cortical surface is compressed during

193 contractile ring assembly, we observed a linear gradient in the velocity of cortical flow that spanned the
194 cell equator in our flow map at early time points prior to furrow ingression (**Figure 3A**). The linear
195 gradient indicated that, during contractile ring assembly when the ring is on the embryo surface, cortical
196 surface is uniformly compressed across a 10 μm wide region along the perpendicular-to-the-ring axis
197 between the two relaxing poles.

198 After its assembly, the ring begins to constrict in the around-the-ring direction, which has been
199 proposed to be coupled to the progressive disassembly of the ring (i.e. loss of components in proportion
200 to reduction in length) (Murrell et al., 2015; Schroeder, 1990). During constriction, the ring pulls the
201 cortex behind it, which leads to a flow of cortex into the division plane. We were interested in whether the
202 compression along the perpendicular-to-the-ring axis is limited to contractile ring assembly, or whether it
203 might also continue during ring constriction. If compression stops, the constricting ring would generate
204 the division plane by pulling the cortex behind it, and the cortical surface area entering the division plane
205 would equal the area of the division plane. In contrast, if compression along the axis perpendicular to the
206 ring continues during constriction, the cortical surface area entering the division plane would be larger
207 than the area of the division plane by the amount of surface compressed.

208 To distinguish between these possibilities, we used the 4D cortical flow map to measure the
209 cortical surface area entering the division plane and compare it to the area of the division plane
210 (accounting for the fact that two surfaces are generated-*red outline in* **Figure 3B**). This analysis revealed
211 that the area of the cortical surface that entered the division plane during ring constriction was
212 significantly greater than the area of the division plane (**Figure 3B**, ***middle panel***). The flux of cortical
213 area into the division plane was 1.5 to 2-fold higher than the rate of change in the area of the division
214 plane throughout cytokinesis, indicating ongoing cortical surface compression (**Figure 3B**, ***right panel***).
215 In control embryos, more cortex flowed in from the posterior side than from the anterior side, likely due to
216 distinct mechanical cortical properties that arise downstream of the polarity machinery. Prior work
217 showed that Arp2/3 inhibition impairs the recruitment of PAR-2 to the posterior cortex and makes myosin
218 and actin dynamics on the posterior cortex more similar to those in embryo anterior (Xiong et al., 2011).
219 Inhibiting the Arp2/3 complex by depleting ARX-2 abolished the difference between the two sides, but did

220 not change the difference between the total amount of cortex entering the division plane and the area of
221 the plane (**Figure 3 – Figure Supplement 1; Video 3**). This result suggests that the compression of
222 cortical surface along the axis perpendicular to the ring persists throughout constriction, resulting in a
223 continuous flow of cortical surface into the ring.

224 Next, we probed the relationship between the rate of cortical surface area compression along the
225 axis perpendicular to the ring and the levels of two contractile ring components, myosin, which is
226 required for ring constriction and cortical surface compression (Reymann et al., 2016; Shelton et al.,
227 1999), and anillin, a filament cross-linker that localizes to the ring but is not essential for constriction or
228 compression (Maddox et al., 2005; Maddox et al., 2007; Reymann et al., 2016). To do this, we monitored
229 *in situ*-tagged myosin::GFP (Dickinson et al., 2013) (**Figure 3C**) and GFP::anillin (**Figure 3 – Figure**
230 **Supplement 2**) in end-on reconstructions of the division plane. Both ring components exhibited similar
231 behavior. Because overall measurements of ring component levels and constriction/compression rates
232 scale with ring size, all of our analysis considers measurements per unit of ring length, which capture the
233 evolution of the material properties of the ring independent of size. Quantification of mean per-unit-length
234 fluorescence around the ring (after attenuation correction; **Figure 3 – Figure Supplement 3**) revealed a
235 steady increase for both markers as constriction proceeded. The increase in the per-unit-length amounts
236 of myosin and anillin began on the top of the ring, which ingresses first, and initiated later on the bottom,
237 which ingresses after the constriction midpoint (**Figure 3C, Figure 3 – Figure Supplement 2**).
238 Comparing the per-unit-length rate of cortical compression along the axis perpendicular to the ring to the
239 per-unit-length amounts of myosin and anillin revealed that both increased with the same exponential
240 kinetics during constriction (**Figure 3C**). Thus, new cortical surface is pulled into the ring due to cortical
241 compression at a rate proportional to the amount of ring myosin. Like the rate of cortical compression
242 along the axis perpendicular to the ring, the per-unit-length constriction rate also increased in proportion
243 to the per-unit-length amount of myosin (**Figure 3C**). The exponential increase in the per-unit-length
244 constriction rate explains the observed ability of the contractile ring to close at a relatively constant rate
245 despite its progressively decreasing perimeter (Bourdages et al., 2014; Carvalho et al., 2009; Zumdieck
246 et al., 2007). A relatively constant overall rate of ring closure is observed over a significant portion of

247 constriction (**Figure 1A**; $t = 50\text{-}200$s) because the exponential increase in the constriction rate balances
248 the decrease in ring size.

249 We note that in prior work in 4-cell stage *C. elegans* embryos, we had shown that myosin, anillin
250 and septins levels in the ring increase ~1.3-fold as ring perimeter decreases 2-fold (from 50 to 25 μm),
251 but had not concluded that contractile ring component accumulation was exponential. This is because
252 the range of ring sizes between furrow formation and contact with the midzone, which occurs at a
253 perimeter of ~25 μm and alters ring properties (Carvalho et al., 2009), is much smaller at the 4-cell stage
254 than at the 1-cell stage. Although not sufficient to demonstrate exponential accumulation on their own,
255 the 4-cell data are well fit by the same exponential equation that describes myosin and anillin
256 accumulation at the 1-cell stage (**Figure 3 – Figure Supplement 4**), suggesting that ring components
257 accumulate in a similar fashion across the first four cell divisions in the *C. elegans* embryo.

258

259 ***An analytical mathematical model for positive feedback-mediated evolution of the contractile***
260 ***ring: the Compression Feedback model***

261 From our experimental work we conclude that: (1) the ring compresses cortical surface along the
262 axis perpendicular to ring constriction throughout cytokinesis at a rate proportional to the amount of ring
263 myosin and, (2) the amount of ring myosin and anillin increase at a rate proportional to the rate at which
264 cortical surface is compressed into the ring, (3) the per-unit-length amounts of ring myosin and anillin and
265 the per-unit-length rates of cortical compression and ring constriction increase with the same exponential
266 kinetics as the ring closes. The fact that ring components accumulate with exponential kinetics further
267 suggests control by positive feedback. Our results suggest that the relevant feedback could be between
268 the amount of ring myosin and the rate of cortical surface compression within the ring (i.e. ring myosin
269 would lead to cortical compression that would deliver myosin into the ring). To explore this idea, we
270 developed an analytical mathematical formulation, which we call the Compression Feedback model,
271 consisting of three equations with three model parameters, that describes this feedback and can
272 recapitulate our experimental results (**Figure 4A,B**).

273 The natural coordinate system for contractile ring dynamics has two axes, an axis parallel to ring
274 constriction (**Figure 4A**, ***around-the-ring axis***) and an axis perpendicular to the ring (**Figure 4A**,
275 ***perpendicular-to-the-ring axis***). Our experimental results suggest that polar relaxation leads to
276 differential behavior in these two directions. After anaphase onset, spindle based signaling patterns the
277 cortex, generating an equatorial zone, that has been termed the Rho zone (Bement et al., 2006; Green
278 et al., 2012; Jordan and Canman, 2012; Piekny et al., 2005), where RhoA promotes the recruitment of
279 contractile ring components including myosin and anillin (Jenkins et al., 2006; Maddox et al., 2005;
280 Maddox et al., 2007; Mangal et al., 2018; Motegi and Sugimoto, 2006; Schonegg et al., 2007; Tse et al.,
281 2012; Werner et al., 2007). The Rho zone occupies the central region of the pole-to-pole axis
282 perpendicular to the ring. As our data indicate (**Figure 3A**), the initial recruitment of contractile ring
283 proteins after anaphase onset results in uniform cortical compression across this central 10 μm wide
284 zone. We propose that, due to polar relaxation, the compressing cortex pulls naïve cortex not patterned
285 by the initial round of RhoA signaling, into the Rho zone (**Figure 4A**). The new cortex that flows into the
286 Rho zone as a result of compression would be loaded with contractile ring components that would initiate
287 compression and contribute to compression-driven cortical flow. Thus, *along the perpendicular-to-the-*
288 *ring* axis a feedback loop would operate in which myosin in the ring compresses cortical surface, which
289 pulls more surface that is loaded with myosin into the ring (**Figure 4A**, left panel). *In the around-the-ring*
290 *direction*, reduction in ring perimeter would be coupled to disassembly (loss of ring components in
291 proportion to reduction in length), with the per unit length rate of ring disassembly being determined by
292 the per unit length amount of myosin. Thus, unlike the feedback loop operating along the perpendicular-
293 to-the-ring axis, which would lead to an exponential increase in the per-unit-length levels of ring
294 components, ring shortening would be coupled to disassembly and would not alter the per-unit-length
295 amount of ring components.

296 In the mathematical formulation (**Figure 4B**), naïve cortex flows into the Rho zone at a velocity
297 ($v_{flow}(t)$) proportional to the per-unit-length amount of ring myosin ($M_{ring}(t)$; **Figure 4B,** Eqn. (1)), with
298 α being the proportionality constant that relates the two. Ring myosin, in turn, increases at a rate
299 proportional to this flow and the concentration of myosin that is loaded onto the cortex when it enters the

rho zone (m_{rho}; **Figure 4B**, Eqn. (2)). As a result of the positive feedback between ring myosin and compression-driven flow, ring myosin increases exponentially with a characteristic time $\tau \coloneqq 1/\alpha m_{rho}$ (time required for ring myosin to increase ~2.7 fold; **Figure 4B, bottom graph**). The per-unit-length rate of ring constriction ($\frac{dR}{dt} * \frac{1}{R}$) is proportional to the per-unit-length amount of ring myosin, related by the proportionality constant β (**Figure 4B,** Eqn. (3)). To avoid the difficulty of accurately assigning the exact point when cytokinesis starts, we solved these equations in the time reference where $t = 0$ is the halfway point of ring closure ($\bar{R}(t = 0) = \frac{1}{2}$). In this time reference, the equation for ring size is:

$$\bar{R}(\bar{t}) = \bar{R}_{ini}(2\bar{R}_{ini})^{-\exp(\bar{t})}, \tag{4}$$

where $\bar{t} \coloneqq t/\tau$ and $\bar{R}_{ini}$ is the dimensionless characteristic ring size (held fixed at a value of 1.1; see Methods; **Figure 4B**, ***right graph***). Other components, like anillin, that localize to the cell cortex will be delivered to the contractile ring via the same process as myosin, and would accumulate in a similar fashion, with

$$C_{ring}(\bar{t}) - C_{ring,base} = \frac{\alpha c_{rho}}{\beta} \ln(2\bar{R}_{ini})\, \mathrm{e}^{\bar{t}}, \tag{5}$$

$$C_{ring,base} \coloneqq C_{0,ring} - \ln(2\bar{R}_{ini}) \frac{\alpha c_{rho}}{\beta}, \tag{6}$$

where $C_{0,ring}$ is the per-unit-length amount of the component at the half-way point of ring closure, $C_{ring,base}$ is the baseline amount of the ring component that does not increase exponentially, and c_{rho} (m_{rho} for myosin) is the concentration of the component loaded onto naïve cortex when it enters the rho zone. The velocity of cortical flow and the constriction rate are

$$v_{flow}(\bar{t}) = \frac{\alpha}{\beta} \ln(2\bar{R}_{ini})\, \mathrm{e}^{\bar{t}}, \tag{7}$$

$$-\frac{1}{\bar{R}} \frac{d\bar{R}}{d\bar{t}} = \ln(2\bar{R}_{ini})\, \mathrm{e}^{\bar{t}}. \tag{8}$$

Thus, the per-unit-length constriction rate, velocity of cortical flow, and ring component amounts would all increase exponentially with the characteristic time of ring myosin accumulation ($\tau = 1/\alpha m_{rho}$) set by the feedback loop between ring myosin and cortical flow, as we have observed experimentally

318 (**Figure 3C**). We conclude that an analytical mathematical formulation that describes a feedback loop
319 between ring myosin and compression-driven cortical flow can recapitulate the experimentally observed
320 pattern of cortical surface compression and ring component and constriction dynamics.
321

322 ***Fluorescence recovery after photobleaching of the division plane is consistent with the***
323 ***Compression Feedback model***

324 The Compression Feedback model is characterized by anisotropy in the behavior in the
325 perpendicular-to-the-ring and around-the-ring directions (**Figure 5A**). Along the perpendicular-to-the-ring
326 direction, cortical compression within the ring pulls in cortical surface, which increases the per-unit-length
327 amount of ring components and, as a consequence, the per-unit-length constriction rate. In contrast, in
328 the around-the-ring direction, constriction is coupled to disassembly and does not affect the per-unit-
329 length amount of ring components. An alternative model that could explain the increase in the per-unit-
330 length amount of ring components, which we refer to as "Retention" model, is that the per-unit-length
331 constriction rate accelerates due to retention of myosin and/or other ring components during ring
332 shortening (**Figure 5A**). In the Retention model, compression in the around-the-ring direction increases
333 the per-unit-length amount of ring components. In this model, myosin and anillin would not be lost due to
334 disassembly, and their total amounts in the ring would remain constant during constriction, resulting in an
335 increase in their per-unit-length amounts in inverse proportion to the reduction in ring size (levels would
336 increase as $\frac{1}{R}$). In the perpendicular-to-the-ring direction, compression would still pull cortical surface into
337 the ring, as we have shown occurs experimentally, but the Retention model assumes that flow would not
338 deliver myosin into the ring, either because levels of myosin on the delivered cortex are insignificant
339 relative to the amount of myosin in the ring or because the delivered myosin is lost due to disassembly.
340 Comparison with the total amounts of ring myosin and anillin suggested that, whereas the Retention
341 model fit the data well for t/t_{ck} between 0.2 and 0.6, there was significant deviation for timepoints
342 outside of this range. In contrast, the Compression Feedback model fit the data well over the entire
343 measured interval (t/t_{ck}= 0.0 to 0.8; **Figure 5B**, **Figure 5—Figure Supplement 1**). The exponential
344 accumulation predicted by the Compression Feedback model also fit the experimental data for the per-

345 unit-length rates of ring shrinkage and cortical compression significantly better than the Retention model,
346 which would predict that these rates, like the amount of ring myosin, would also increase as $\frac{1}{R}$ (**Figure**
347 **5B**).

348 As a further test of the Retention and Compression Feedback models, we photobleached myosin
349 in the entire division plane at ~30% closure, and monitored its subsequent recovery in the ring (**Figure**
350 **6A**). In prior work, we photobleached three contractile ring components (myosin::GFP, GFP::anillin, and
351 GFP::septin) in contractile rings at the 4-cell stage. This analysis suggested that in contrast to myosin on
352 the cortex outside of the ring, which has been shown to turn over rapidly ($t_{1/2}$ of ~30s; (Mayer et al., 2010;
353 Salbreux et al., 2012)), significant turnover due to exchange with components in the cytoplasm was not
354 observed for myosin, anillin, or the septins in the ring. The Retention model predicts that cortical
355 compression along the perpendicular-to-the-ring direction does not contribute to ring myosin
356 accumulation. In the around-the-ring direction, the cortex is compressed as ring perimeter decreases
357 leading to an increase in the per-unit-length amount of both the bleached and residual fluorescent
358 myosin in proportion to the reduction in ring perimeter (both would increase as 1/R; (**Figure 6B**, ***top***).
359 The Compression Feedback model predicts that after the myosin in the ring is bleached, cortical
360 compression in the perpendicular-to-the-ring direction will continue to pull continue naive cortex into the
361 Rho zone that will be loaded with fluorescent myosin from the cytoplasm. Thus, after the bleach, the per-
362 unit-length amount of fluorescent myosin in the ring will rapidly begin to increase again at an exponential
363 rate comparable to that in controls. In the around-the-ring direction, the bleached myosin in the ring will
364 be disassembled in proportion to the reduction in ring length; thus, the per-unit-length amount of
365 bleached myosin in the ring will remain constant (**Figure 6B**, ***bottom***). Our data indicated that the per-
366 unit-length amount of fluorescent myosin in the ring increased exponentially following bleaching at a rate
367 comparable to that in controls, and the difference between the fluorescence in the control and bleached
368 embryos, which is the amount of bleached myosin, remained constant as the ring constricted. These
369 observations are consistent with the predictions of Compression Feedback model but not the Retention
370 model (**Figure 6C**). We also note that, consistent with our prior observations at the 4-cell stage (Carvalho
371 et al., 2009) we did not observe evidence of turnover of ring myosin due to exchange with myosin in the

372 cytoplasm. If ring myosin were turning over due to exchange with cytoplasmic myosin, we would expect
373 the curve for fluorescence in the ring after the bleach to approach the control curve and the difference
374 between the two curves to decrease exponentially. Instead, the two curves remained parallel and the
375 difference remained constant (**Figure 6C**). Imaging after bleaching of the entire division plane at the 4-
376 cell stage yielded a very similar result (**Figure 6—Figure Supplement 1)**. We conclude that acceleration
377 of the per-unit-length constriction rate during closure, a conserved feature of contractile rings, does not
378 arise from retention of components in the around-the-ring direction. Our results are instead consistent
379 with the idea that acceleration arises from positive feedback between ring myosin and compression-
380 driven cortical flow along the axis perpendicular to the ring.
381

382 **DISCUSSION**

383 ***The Compression Feedback model: a new explanation for the acceleration in the per-unit-length***
384 ***constriction rate during constriction***

385 Our simultaneous analysis of cortical and contractile ring dynamics suggests a new explanation
386 for the acceleration in the per-unit-length constriction rate that allows contractile rings to maintain a high
387 closure rate despite their progressively decreasing perimeter (Biron et al., 2004; Bourdages et al., 2014;
388 Calvert et al., 2011; Carvalho et al., 2009; Ma et al., 2012; Mabuchi, 1994; Pelham and Chang, 2002;
389 Zumdieck et al., 2007). Rather than arising from an increase in the per-unit-length amount ring myosin
390 due to retention, we propose that acceleration arises from an exponential increase in the per-unit-length
391 amount ring myosin due to feedback between ring myosin and compression-driven cortical flow along the
392 direction perpendicular to the ring (**Figure 7**). In our model, polar relaxation allows ring myosin to
393 compress cortical surface along the pole-to-pole axis perpendicular to the ring, thereby increasing the
394 amount of ring myosin. An increase in the per-unit-length amount of ring myosin, in turn, would lead to
395 increased cortical compression, resulting in a feedback loop that drives an exponential increase in the
396 per-unit-length amount of ring myosin. In this model, the overall amounts of myosin, anillin (and
397 presumably other components) in the ring would remain relatively constant as the ring constricts (**Figure**
398 **5—Figure Supplement 1**) due to a balance between loss due to disassembly-coupled ring shortening
399 and accumulation due to feedback in the perpendicular-to-the-ring direction. Thus, the relatively constant
400 overall levels would mask a dramatic restructuring of the ring during closure. We note that the model we
401 propose here is reminiscent of early conceptual models of cytokinesis, which hypothesized that polar
402 relaxation coupled to a global upregulation of surface tension could trigger a flow of tension-generating
403 elements towards the equator that would compress into a circular band and initiate a feedback loop
404 (Greenspan, 1978; Swann and Mitchison, 1958; Taber, 1995; White and Borisy, 1983; Wolpert, 1960;
405 Zinemanas and Nir, 1987; Zinemanas and Nir, 1988).

406 In addition to ensuring timely cell content partitioning, an advantage of the feedback-based
407 mechanism that we propose here is that it would render the ring robust to internal or external mechanical
408 challenges, such as cell-cell contacts, obstacles in the crowded cell interior, or defects in the cytokinesis

409 machinery. In all of these cases, a feedback loop between ring myosin and compression-based flow
410 along the direction perpendicular to constriction would lead to the progressive build-up of contractile ring
411 components until they reached a level where the obstacle could be overcome and constriction would
412 again be able to proceed. Concentrating components by compression in the around-the-ring direction
413 would not have this property, since successful constriction would be required to increase component
414 levels. We note that similar ring-directed cortical flows have also been observed in the context of wound
415 healing (Mandato and Bement, 2003), where they could potentially serve a similar function in allowing
416 the cell to ramp up contractile force and achieve wound closure.

417 The experimental basis for our model is our analysis of cortical dynamics, which indicates that the
418 compression of cortical surface within the ring along the axis between the relaxing poles that initiates
419 during contractile ring assembly (Figure 3; (Reymann et al., 2016)), persists throughout constriction,
420 resulting in a continuous flow of cortical surface into the ring. A second key finding is that the per-unit-
421 length amount of ring myosin and anillin and the per-unit-length rates of cortical compression and ring
422 constriction increase with the same exponential kinetics, suggesting control by positive feedback. We
423 note that it remains possible that there is a distinct source of positive feedback (other than between ring
424 myosin and cortical compression as we propose) that controls myosin recruitment, and that myosin
425 levels in turn control the rates of constriction and cortical compression. However, since our data indicate
426 that cortical surface is compressed within the ring, such a model would need to invoke an as yet
427 uncharacterized process to explain why compression of the cortex within the ring would not increase the
428 concentration of ring components. We note that compression within the ring along the direction
429 perpendicular to the ring is also consistent with work in *S. pombe*, which has shown that contractile ring
430 assembly occurs via a similar acto-myosin based compression of an equatorial band of nodes into a
431 compact ring along the long axis of the cell (Vavylonis et al., 2008; Wu et al., 2006). However, in contrast
432 to *pombe* where ring assembly and constriction occur in distinct phases, our model predicts that in
433 animal cells, the accumulation of ring components due to compression along the direction perpendicular
434 to the ring is ongoing, and serves to accelerate the per-unit-length constriction rate as the ring closes.
435

436 ***Polar relaxation enables cortical compression within the ring along the pole-to-pole axis***

437 Monitoring cortical dynamics in combination with laser ablation experiments revealed that the
438 polar cortex is distinct from the cortex in the region between the contractile ring and the poles. The polar
439 cortex expands in response to tension generated by the constricting ring, whereas the intervening cortex
440 flows towards the ring without expanding. One possibility is that polar cortex is less stiff than the rest of
441 the cortex, causing it to stretch and thin in response to ring constriction-induced tension. Alternatively,
442 the polar cortex could turnover more rapidly, leading to a higher rate of surface renewal after stretching.
443 A third possibility is that the polar cortex is more prone to rupture, repair of which would locally increase
444 cortical surface. Consistent with this last idea, blebs have been reported at the cell poles in cultured
445 vertebrate and *Drosophila* cells, where they have been proposed to release tension at the poles (Hickson
446 et al., 2006; Sedzinski et al., 2011). The distinct mechanical properties of the polar cortex suggest that its
447 composition could be different from that of the adjacent cortex. This idea is consistent with both older
448 work suggesting the existence of mechanisms that clear contractile ring proteins from the poles (Bement
449 et al., 2005; Chen et al., 2008; Foe and von Dassow, 2008; Murthy and Wadsworth, 2008; von Dassow,
450 2009; Werner et al., 2007; Zanin et al., 2013) and recent studies that have begun to uncover molecular
451 mechanisms that may drive clearing. Work in *C. elegans* has demonstrated the existence of a
452 mechanism in which Aurora A, localized to astral microtubules by association with its activator TPXL-1,
453 actively clears contractile ring proteins from the polar cortex (Mangal et al., 2018). A reduction in f-actin
454 intensity at the cell poles due to delivery of a phosphatase by segregating chromosomes has also been
455 reported in *Drosophila* cells (Rodrigues et al., 2015). Understanding how the polar cortex is different in
456 molecular and mechanical terms, and the mechanisms that generate these differences are important
457 goals for future work.

458 Cleaving sea urchin embryos exhibit constriction kinetics essentially identical to those during the
459 first division of the *C. elegans* embryo (Mabuchi, 1994). Pioneering work measuring the distance
460 between surface-adhered particles and the behavior of pigmented cortex-associated granules (Dan,
461 1954; Dan and Dan, 1940; Dan et al., 1938), indicated that sea urchin embryos also exhibit a similar
462 pattern of cortical expansion during ring constriction, in this case, a wave of cortical expansion that

463 initiates at the poles and propagates through to the region adjacent to the furrow (Dan et al., 1938; Dan
464 and Ono, 1954; Dan et al., 1937; Gudejko et al., 2012; Swann and Mitchison, 1958). Cortical
465 compression and expansion have not been mapped in vertebrate cells; however, monitoring of
466 fluorescent latex spheres adhered to cell surface proteins (Fishkind et al., 1996; Wang et al., 1994),
467 injected stabilized fluorescent actin filaments (Cao and Wang, 1990), and fluorescently labeled myosin II
468 (DeBiasio et al., 1996) all revealed concerted cortical flow towards the division plane in the equatorial
469 region of the cell that contrasted with random surface movements at the cell poles. These observations
470 suggest that feedback in which relaxation enables compression-driven cortical flow may be a conserved
471 feature of animal cell cytokinesis.
472
473 ***The Compression Feedback model predicts that the evolution of component levels in the ring***
474 ***during constriction requires both de novo recruitment and compression-driven cortical flow***
475 It is worth noting that our proposed model represents an interesting twist on an ongoing debate in
476 the cytokinesis field as to whether contractile ring components are delivered into the ring via cortical flow
477 (Cao and Wang, 1990; DeBiasio et al., 1996; Fishkind et al., 1996; Wang et al., 1994) or recruited de
478 novo from the cytoplasm downstream of RhoA-based signaling (Vale et al., 2009; Yumura, 2001; Zhou
479 and Wang, 2008). In the Compression Feedback model, we propose that following anaphase onset
480 contractile ring components are initially recruited to the equatorial cortex de novo, as has been observed
481 (Vale et al., 2009; Yumura, 2001; Zhou and Wang, 2008), but then component levels are amplified by a
482 feedback loop in which compression of cortical surface in the ring pulls new cortex into the Rho zone that
483 is then loaded de novo with contractile ring components. Thus, during the exponential increase in the
484 per-unit-length amount of ring components, compression-driven flow of new cortex into the Rho zone
485 would be required for the subsequent de novo loading of contractile ring components. We would
486 therefore propose that both the de novo loading of components by Rho-based signaling and
487 compression-driven flow could contribute to the evolution of the component levels in the ring during
488 constriction.
489

490 ***The Compression Feedback model as a tool to describe the feedback-mediated evolution of the***
491 ***contractile ring***

492 To quantitatively explore the idea that a feedback loop between the amount of ring myosin and
493 compression-driven flow of cortical surface into the ring drives component accumulation during
494 constriction, we developed an analytical mathematical framework, which we call the Compression
495 Feedback model. The Compression Feedback model consists of three equations with three model
496 parameters that describes this feedback and can recapitulate our experimental results. In addition to
497 describing the processes underlying the evolution of the contractile ring, the Compression Feedback
498 model provides a simple framework that can be used to analyze the consequences of molecular
499 perturbations. Since the Compression Feedback model accurately describes the dynamics of the
500 contractile ring and associated cortical network, an additional interesting future direction will be to use
501 parameter changes derived from the Compression Feedback model as input for a finite-element model
502 (similar to (Turlier et al., 2014)) in order to predict the evolution of cell shape given an *a priori* knowledge
503 of cortical and contractile ring dynamics.
504

505 **METHODS**

506 ***C. elegans strains used in this study***

Strain Name	Genotype	Reference
OD821	*ltSi200[pOD1997; Pnmy-2::nmy-2::gfp; cb-unc-119(+)] II; unc-119(ed3) III*	This study
OD857	*ltSi200[pOD1997; Pnmy-2::nmy-2::gfp; cb-unc-119(+)] II; unc-119(ed3); ruIs32[pAZ132; pie-1/GFP::histone H2B] III*	This study
OD858	*ltSi803[pOD1998; Parx-7::GFP::arx-7; cb-unc-119(+)] II; unc-119(ed3) III;*	This study
LP162	*nmy-2(cp13[nmy-2::gfp + LoxP]) I*	(Dickinson et al., 2013)
OD95	*unc-119(ed3) III; ltIs37 [pAA64; Ppie-1::mCherry::his-58; unc-119(+)] IV; ltIs38 [pAA1; Ppie-1::GFP::PH(PLC1delta1); unc-119 (+)]*	(Essex et al., 2009)
OD3011	*ltSi1123[pSG017; Pani-1::GFP::ani-1 RE-encoded-exon5::ani-1 3'-UTR; cb unc-119(+)]II;unc-119(ed3)III*	This study
GOU2047	*cas607[arx-2::gfp knock-in] V*	(Zhu et al., 2016)

507

508 The *C. elegans* strains listed in the table were maintained at 20°C using standard methods. OD821
509 and OD858, expressing NMY-2::GFP, GFP::anillin, and GFP::ARX-7 were generated using a
510 transposon-based strategy (MosSCI; (Frokjaer-Jensen et al., 2008)). Genomic regions encoding *nmy-2*
511 (including 2079 bp and 1317 bp up and downstream of the stop codon, respectively), *ani-1* (including
512 2015 bp and 1215 bp up and downstream of the stop codon), and *arx-7* (including 3056 bp and 634 bp
513 up and downstream of the stop codon) were cloned into pCFJ151 and sequences encoding GFP were
514 inserted either just before (*nmy-2*) or after (*arx-7* and *ani-1*) the start codon. The single copy *nmy-2*
515 transgene was generated by injecting a mixture of repairing plasmid (pOD1997, 50ng/μL), transposase
516 plasmid (pJL43.1, Pglh-2::Mos2 transposase, 50ng/μL), and fluorescence selection markers (pGH8,
517 Prab-3::mCherry neuronal, 10ng/μL; pCFJ90, Pmyo-2::mCherry pharyngeal, 2.5ng/μL; pCFJ104, Pmyo-
518 3::mCherry body wall, 5ng/μL) into EG6429 (ttTi5605, Chr II). Single copy *ani-1* and *arx-7* transgenes
519 were generated by injecting a mixture of repairing plasmid (pSG017 (*ani-1*) or pOD1998 (*arx-7*),
520 50ng/μL), transposase plasmid (CFJ601, Peft-3::Mos1 transposase, 50ng/μL), selection markers (same
521 as for *nmy-2* strain) and an additional negative selection marker (pMA122; Phsp-16.41::peel-1, 10ng/μL)
522 into EG6429 (ttTi5605, Chr II). After one week, progeny of injected worms were heat-shocked at 34°C for

523 2-4 hours to induce PEEL-1 expression and kill extra chromosomal array containing worms (Seidel et al.,
524 2011). Moving worms without fluorescent markers were identified and transgene integration was
525 confirmed in their progeny by PCR spanning both homology regions in all strains.
526
527 **C. elegans *RNA-mediated interference***
528 Double stranded RNA (dsRNA) targeting *arx-2* (K07C5.1) at a concentration of 1.7 mg/ml was
529 generated by synthesizing single-stranded RNAs in 50μL T3 and T7 reactions (MEGAscript, Invitrogen,
530 Carlsbad, CA) using cleaned DNA template generated by PCR from N2 DNA using the oligos
531 (TAATACGACTCACTATAGGTCAGCTTCGTCAAATGCTTG and
532 AATTAACCCTCACTAAAGGTGCAATACGCGATCCAAATA). Reactions were cleaned using the
533 MEGAclear kit (Invitrogen, Carlsbad, CA), and the 50 μL T3 and T7 reactions were mixed with 50μL of
534 3× soaking buffer (32.7mM Na_2HPO_4, 16.5mM KH_2PO_4, 6.3mM NaCl, 14.1mM NH_4Cl), denatured at
535 68°C for 10min, and then annealed at 37°C for 30 min to generate dsRNA. L4 hermaphrodite worms
536 were injected with dsRNA and allowed to recover at 16°C for 44-50 hours prior to imaging.
537
538 ***Generating a 4D map of cortical flow***
539 Cortical flow was monitored in embryos expressing myosin::GFP obtained from adult
540 hermaphrodites by dissection. Embryos were mounted followed by sealing with a coverslip on double
541 thick (1 mm) low percentage agarose (0.5%) pads to prevent compression that biases the initial angle of
542 furrow ingression (**Figure 1 – Figure Supplement 1B**). Images were acquired on an inverted
543 microscope (Axio Observer.Z1; Carl Zeiss) equipped with a spinning-disk confocal head (CSU-X1;
544 Yokogawa) and a 63× 1.40 NA Plan Apochromat lens (Zeiss) using a Hamamatsu Orca-ER digital
545 camera (Model C4742-95-12ERG, Hamamatsu photonics). Images were collected using custom
546 software, written in Python, that utilizes the Micro-Manager (open source software, (Edelstein et al.,
547 2014)) microscope control library. A 3 x 0.75 μm z-series was collected (400ms exposure, 10-20% laser
548 power) every 2s. After 15 time points, a 15 x 1μm z-stack, offset by 3μm from the cortical surface, was
549 imaged to monitor the position of the closing contractile ring. The entire imaging series was repeated

550 every 36s until the end of cytokinesis. Cortical flow was measured in maximum intensity projections of
551 the 3 x 0.75μm z-stacks of the cortical surface, after orientation of the images to place the embryo
552 anterior at the top and the posterior at the bottom, by correlating myosin fluorescence between
553 consecutive images using Gunnar Farnebäck's algorithm (Farnebäck, 2003) implemented within the
554 openCV library with a 30-pixel window size. The threshold was calculated for every image by maximizing
555 the ratio of total intensity inside a 200x350 pixel box positioned in the center of the embryo to the total
556 intensity outside that box.
557
558 ***Measurement of contractile ring position and size***
559 Automated methods were employed to identify the edges of the embryo, determine the position of
560 the contractile ring, and reconstruct the rings for each time point in an end-on view to determine the initial
561 ingression axis (**Figure 1 – Figure Supplement 2**). Ring size and position were determined using
562 custom Python software that: (1) identifies the orientation of the anterior-posterior (AP) axis and rotates
563 the embryo to place the embryo anterior at the top and the embryo posterior at the bottom, (2) finds the
564 embryo center in different x-z planes along the AP axis and calculates embryo radius, and (3) calculates
565 the radius of the contractile ring and determines its position within the division plane. Details of each step
566 are outlined below.
567 Orienting embryos with their anterior end to the top: Acquired z-plane images were convolved with a
568 10-pixel Gaussian kernel to reduce noise. An optimal signal threshold that partitioned the embryo interior
569 from exterior was identified by finding a local minimum in the intensity histogram that produced a binary
570 mask with expected area (~120000±50000 pixel^2). The orientation of the AP axis was identified by fitting
571 an ellipse to the thresholded area in the middle plane of the z-stack. The anterior side was identified by
572 higher cortical myosin fluorescence and all images were rotated to place the embryo anterior at the top of
573 the image and the embryo posterior at the bottom.
574 Defining the central axis of embryo and determining embryo width: The central axis of the embryo
575 was defined by drawing a horizontal line across the oriented embryo at the midpoint between its anterior
576 and posterior ends and identifying the first and last points along this line with signal above the threshold

577 for each z-plane. The identified pixels were virtually projected in an end-on (x-z) view and fit to a circle by
578 minimizing residuals. To account for fluctuations in the embryo boundary due to noise and fluorescence
579 variation, the procedure was repeated 9 more times after shifting the position of the horizontal line
580 towards the anterior pole by 10 pixels, covering approximately 1/5 of the embryo length (500 pixels). The
581 position of the AP axis and the radius of the embryo were determined by averaging the 10
582 measurements.

583 Measuring contractile ring size and position: As illustrated for the central plane images shown in
584 Figure 1 – Figure Supplement 2, the position of the contractile ring was determined by identifying pairs of
585 points with the highest myosin fluorescence intensity on the opposite edges of the embryo in each z-
586 plane that were not more than 20 pixels apart in the horizontal direction and were located at a y-axis
587 position near the embryo middle. Contractile ring radius and position were determined by projecting the
588 points to generate an end-on (x-z) view and fitting the data with a circle. The ring fit was iteratively
589 improved by calculating predicted positions of myosin fluorescence at the ring in each z-plane using
590 initially fitted parameters. Intensity maxima within 5 pixels of the predicted location were identified and
591 the ring was refit. The initial guesses for the contractile ring size and position at the next time point were
592 estimated from the previously calculated ring values. The algorithm restricted ring position fluctuations to
593 20 pixels along anterior-posterior axis and the size was estimated assuming constant rate of ring
594 constriction. The automatic ring measurements were manually confirmed for each embryo. The initial
595 ingression axis was determined as illustrated (**Figure 1 – Figure Supplement 2**) by fitting a line through
596 the centers of the rings with a normalized ring size ($\bar{R} := R/R_{emb}$) > 0.3.

597

598 ***Embryo time alignment for averaging***

599 Sequences from individual embryos were time aligned by defining zero time (t_0) and the total time
600 of cytokinesis (t_{CK}) for each embryo, and normalizing time by t_{CK} prior to averaging, $\hat{t} := \frac{t-t_0}{t_{CK}}$. An initial
601 determination of t_0 and t_{CK} was made by fitting a line to the plot of normalized ring size ($\bar{R}(t) := R/R_{emb}$)
602 versus time between 30% and 80% closure for each embryo as outlined in Figure 1A. Extrapolation of
603 this line for each embryo defined t_0 as the time where the fitted line intersects 1, and the time of

604 cytokinesis, t_{CK} as the time where the fitted line intersects 0. Due to the small number of measurements
605 from each embryo available for fitting (3-5 values where 0.8> $\bar{R}$ >0.3), the values of t_0 and t_{CK} were
606 refined by fitting $\bar{R}(\hat{t})$ for each embryo to the average dimensionless ring size, $< \bar{R} > (\hat{t})$. Calculation of
607 the average dimensionless ring size was performed in iterative manner. The time for each embryo was
608 aligned by t_0 and normalized by t_{CK} using estimates from the fitted line in the first iteration. The average
609 dimensionless ring size ($< \bar{R} > (\hat{t})$) was calculated by averaging normalized ring sizes of all embryos at
610 corresponding normalized time. Contractile ring size was approximated for intermediate time points by
611 linear interpolation. In further iterations, t_0 and t_{CK} were refined for every embryo by minimizing the
612 residuals between its normalized ring size, $\bar{R}(\hat{t})$, and the average dimensionless ring size, $< \bar{R} > (\hat{t})$,
613 throughout the entire timecourse of cytokinesis, thus increasing the number of time points available for
614 fitting t_0 and t_{CK} (6-10 values per embryo). After refining time alignment and normalization for each
615 embryo, average dimensionless ring size was re-calculated and t_0 and t_{CK} were refined for each embryo
616 again. The refinement process was repeated until changes in average dimensionless ring size, $< \bar{R} >$
617 $(\hat{t})$, were smaller than 0.001 on average (achieved within a few iterations). The collective fitting of all t_0
618 and t_{CK} at every iteration was performed under restriction that the line fit through $< \bar{R} > (\hat{t})$ between 0.8
619 and 0.3 intercepted 0 at $\hat{t} = 0$ and 1 at $\hat{t} = 1$. This restriction ensured that t_0 and t_{CK} determined from fits
620 of individual embryos to the average ring size would be consistent with their original definition. The
621 dimensional ring kinetics, $< R > (t)$, can be recovered using the following equation

$$< R > (t) = < R_{emb} >< \bar{R} > (\hat{t} < t_{CK} >), \quad (9)$$

622 where $< R_{emb} >= 14.7 \pm 0.7\ \mu m$ and $< t_{CK} >= 200\ \pm 30\ s$ are average embryo radius and time of
623 cytokinesis accordingly.

624
625 ***Cortical flow averaging***

626 Cortical flow averaging was performed after spatial and temporal alignment of data collected in
627 different embryos (n=93 embryos from 93 worms filmed over the course of 5 days for control, **Video 2**;
628 n=68 embryos from 68 worms filmed over the course of 4 days for *arx-2(RNAi)*, **Video 3**). The number of
629 embryos was chosen to achieve at least 10-fold coverage for all areas of the cortical map for controls

630 and 5-fold coverage for *arx-2(RNAi)*. Linear interpolation was used to approximate the flow between
631 consecutive time points. Because our imaging regime required periodic z-stack acquisition to determine
632 the trajectory of ring closure, no flow approximation was done during those time periods (~6s gap every
633 30s). The flow data for each time point was represented as a set of vectors with direction and magnitude
634 corresponding to the direction and magnitude of the cortical flow at the base of the vector. The base of
635 each vector had two spatial coordinates: x, the position along the anterior-posterior axis (where the
636 position of the contractile ring was defined as 0), and θ, the angular position relative to the initial
637 ingression axis (defined as described in **Figure 1A and Figure 1 – Figure Supplement 2**). We note that
638 mitotic exit is accompanied by a brief (~50-60s) period of rotational flow ((Naganathan et al., 2014;
639 Schonegg et al., 2014); see **Video 1**), which dissipates soon after initiation of cytokinesis (~$\hat{t}$=0.2-0.3).
640 As this rotational contribution is not relevant here, we removed it by averaging the data from the right and
641 left halves of the embryo (in an end-on view), allowing us to focus on rotation-independent flows. Thus,
642 the flow with angular positions greater than 180 degrees was mirrored in angular direction

$$f_{\theta}(\hat{t}, x, \theta > 180) \;\rightarrow\; -f_{\theta}(\hat{t}, x, 360 - \theta), \tag{10}$$

643 f_{θ} is the angular component of the flow vector $\vec{f}$. The flows were normalized by the embryo size and
644 cytokinesis rate $\vec{\bar{f}}(\hat{t}, x, \theta) \coloneqq \frac{t_{CK}}{R_{emb}} \vec{f}(\hat{t}, x, \theta)$ and averaged according to its position and time

$$< \vec{\bar{f}} > (\hat{t}, x, \theta) = \frac{\sum_{emb} \vec{\bar{f}}(\hat{t}, x, \theta)}{N_{emb}}. \tag{11}$$

645

646 ***Calculation of expected cortical surface flow profiles***

647 To aid in the interpretation of experimental results, expected profiles for cortical surface movement were
648 calculated for defined patterns of cortical surface increase and plotted (**Figure 1B and Figure 1 – Figure**
649 **Supplement 3**). The general form of surface movement velocity is given by the following equation

$$v(x) = \int_0^x g(x')dx' + u, \tag{12}$$

650 where $g(x)$ is the amount of cortical surface gain and u is the velocity of asymmetric ring movement,
651 which could be positive or negative, depending on whether the ring is moving towards or away from the
652 surface. From equation (12) we obtain the following predictions

653 Uniform surface increase: $v(x) = Cx + u$;

654 Polar surface increase: $v(x) = C + u$;

655 Behind the ring surface increase: $v(x) = u$ (if the asymmetry of cytokinetic furrowing arises due to
656 global surface movement) or $v(x) = 0$ (if the asymmetry in surface increase is related to the asymmetric
657 furrowing).

658

659 ***Cortical laser ablation***

660 Cortical laser ablations, presented in Figure 2, were performed using a robotic laser microscope
661 system (RoboLase) (Botvinick and Berns, 2005). Embryos expressing myosin::GFP were mounted using
662 standard procedures. A cortical cut, approximately 10 μm long, was made on the anterior side of the
663 embryo when the ring was at ~50% closure (7μm radius). The cut was confirmed by comparison of
664 cortical fluorescence images before and after the cut and was considered successful if the foci moved
665 away from the cut area (~3.5μm distance), indicating cortical tension release. Contractile ring closure
666 rate was calculated by measuring the difference in ring sizes before and after the cut, assessed from two
667 4x2μm z-stacks acquired immediately before the cut and 13s later. Errors in measuring the radius at the
668 two timepoints were determined from the procedure used to fit the data to a circle and were propagated
669 to determine the errors in the constriction rate measurements for individual embryos; mean errors are
670 S.E.M. The cortical opening after ablation was approximately 35μm^2; this translates into an additional
671 reduction in ring radius by ~0.8μm, if the cortical surface tension dominates the ring closure rate. This
672 additional decrease in ring size within 13s should correspond to increase of the control rate (0.22μm/s)
673 by ~30% (0.06μm/s). The experiment was repeated 19 times for no cut condition, 14 times for parallel
674 cut, and 15 times for perpendicular cut. All imaging was performed over the course of 5 days. The
675 number of embryos was chosen to achieve sufficient accuracy in the determination of mean ring closure
676 rates to assess whether it was altered by the cuts.

677

678 ***Calculation of the surface area flowing into the division plane***

679 We calculated the amount of surface area flowing into the division plane from flow measurements
680 made 7 μm away from the position of the furrow on the anterior and posterior sides (as illustrated in
681 **Figure 3B**). The rate of the surface flow is

$$\frac{dA_{surf}}{d\hat{t}}(\hat{t}) = 2R_{emb}\int_0^{\pi} < \vec{f} > (\hat{t}, x_0, \theta)d\theta \ , \tag{13}$$

682 where x_0 is -7 μm and 7 μm for the rate of flow from the anterior or the posterior sides, respectively. The
683 total amount of surface area that entered the division plane from any time $\hat{t}_0$ to $\hat{t}$ is obtained by
684 integrating equation (13) over time

$$A_{surf}(\hat{t}) = \int_{\hat{t}_0}^{\hat{t}} \frac{dA_{surf}}{d\hat{t}}\bigg|_{ant} + \frac{dA_{surf}}{d\hat{t}}\bigg|_{post}(t')dt'. \tag{14}$$

685 The increase in area of the division plane was calculated as following

$$A_{div\ plane}(\hat{t}) = 2\pi(< R >^2 (\hat{t}_0) - < R >^2 (\hat{t})). \tag{15}$$

686 In Figure 3B we used $\hat{t}_0 = -0.2$. The cortical surface area compressed in the ring can be inferred from
687 the difference between the surface area entering the division plane and the area of the division plane

$$A_{comp}(\hat{t}) := A_{surf}(\hat{t}) - A_{div\ plane}(\hat{t}). \tag{16}$$

688

689 ***Division plane imaging***

690 For quantification of myosin::GFP and GFP::anillin amounts in the contractile ring, adult worm
691 dissection and one-cell stage embryos imaging was performed in a custom microdevice (Carvalho et al.,
692 2011). The device was mounted on an inverted microscope (Axio Observer.Z1; Carl Zeiss) and embryos
693 were imaged with a 63x1.4NA Plan Apochromat objective using an electron-multiplying charge-coupled
694 device camera (QuantEM:512SC, Photometrics; 100ms exposure, EM gain set to 500, 10% laser
695 power). Division planes were reconstructed from 40 x 0.5μm z-stacks collected every 30s after
696 background subtraction and attenuation correction. All imaging was done at 20°C.

697

698 ***Contractile ring photo-bleaching and imaging***

699 1-cell stage embryos were mounted in microdevices as for division plane imaging and 4-cell stage
700 embryos were mounted on slides with 2% agarose pads. Embryos were imaged on a Nikon TE2000-E
701 inverted microscope equipped with a 60x1.40NA objective, an EM-CCD camera (iXon; Andor
702 Technology; EM-Gain=220, Exposure =100ms), and a krypton-argon 2.5 W water-cooled laser. For 1-cell
703 stage embryos, division planes were reconstructed from 30x1μm stacks acquired every 20s with 20%
704 laser power and photo-bleaching was performed by 2 sweeps of a 488nm laser with 100% power and
705 500μs dwell time. For 4-cell stage embryos, division planes were reconstructed from 16x1μm stacks
706 acquired every 10s with 50% laser power and photo-bleaching was performed by 2 sweeps of a 488nm
707 laser with 100% power and 100μs dwell time. For 4-cell stage embryos, the time between the
708 prebleached and first postbleached images was 6s.
709
710 ***Estimation of depth attenuation***
711 To estimate depth attenuation within the division plane, we quantified the intensity of the division
712 plane in two cell embryos expressing a GFP-tagged probe expected to be uniformly present on the
713 plasma membrane. From each image, we subtracted a background intensity calculated as the average
714 value inside two 11x11 μm rectangles positioned 2 μm away from the division plane inside the anterior
715 and posterior cells (**Figure 3 – Figure Supplement 3**). The division plane intensity profile was obtained
716 by performing a 30 pixel maximum intensity projection along the AP axis, with the division plane
717 positioned approximately in the middle (**Figure 3 – Figure Supplement 3**). The intensity profiles in z
718 from 13 embryos were fitted to an exponential using the same characteristic attenuation depth for all
719 embryos

$$I = I_0 e^{-z/z_{att}}, \tag{17}$$

720 which yielded a characteristic depth of attenuation, z_{att}, of 15 μm.
721
722 ***Quantification of myosin and anillin intensity in the contractile ring and on the cortex***
723 For embryos at the 1-cell stage, myosin::GFP and GFP::anillin intensities in the contractile ring and
724 on the cortex were quantified in 40x0.5 μm z-stacks containing the ring after correction for depth

725 attenuation and subtraction of background fluorescence. Average intensity along the ring was calculated
726 across a set of embryos in 30 degree arcs (for myosin::GFP, n=36 embryos from 18 worms filmed over 5
727 days; for anillin::GFP, n= 26 embryos from 14 worms filmed over 4 days). The number of embryos was
728 chosen to determine mean fluorescence with sufficient accuracy to derive appropriate conclusions.
729 Positions along the ring were referenced based on the angle between the line from the position on the
730 ring to the ring center and the initial ingression axis. Linear interpolation in time was used for every
731 embryo to estimate intensity in the intermediate time points to perform averaging. Measured intensities
732 were divided by arc length and averaged between different embryos to obtain mean GFP fluorescence
733 per-unit-length for different angular ranges and the average for all angles. Total ring GFP fluorescence
734 was calculated by integrating over ring perimeter. Cortical intensities were quantified by choosing the
735 time point with the ring size closest to $\bar{R} = 0.8$ and measuring total fluorescence in the 15th plane after
736 correction for depth attenuation and subtraction of background fluorescence.

737 Measurements of myosin::GFP fluorescence in the ring at the 4-cell stage were performed as
738 described in Carvalho et. al., 2009. However background fluorescence was determined as the mean
739 fluorescence within a variable size circle at least 10 pixels in diameter, instead of fixed at 10 pixels, to
740 improve measurement quality.

741
742 ***Derivation of the Compression Feedback model for cytokinesis***

743 The Compression Feedback model formalizes the following conceptual view of cytokinesis: After
744 anaphase onset spindle based signaling patterns the cortex, generating an equatorial zone where RhoA
745 promotes the recruitment of contractile ring components (the Rho zone). Within the Rho zone, myosin
746 engages with actin to exert an isotropic force that compresses the cortical surface, resulting in uniform
747 compression across this region, as is observed experimentally (**Figure 3A**). Due to polar relaxation, the
748 compressing cortex pulls naïve cortex not previously patterned by RhoA signaling into the Rho zone. We
749 propose that the new cortical surface that flows into the Rho zone as a result of compression is also
750 loaded with contractile ring components. Thus, a feedback loop is established along the direction
751 perpendicular to the ring, in which myosin in the ring compresses cortical surface, which pulls more
752 surface that is loaded with myosin into the ring. Disassembly in the around-the-ring direction reduces ring

components in proportion to the reduction in length, and does not alter the per-unit-length amount of myosin. Thus, changes in myosin levels are determined solely by the flow of naïve cortex into the Rho zone along the direction perpendicular to the ring, which can be solved as a one-dimensional problem. We assume that the rate of compression of cortical surface (between x and $x + dx$) is proportional to local myosin concentration, $m(x,t)$, which exerts stress onto the actin network resulting in

$$\frac{\delta\varepsilon}{\delta t}(x,t) = -\alpha m(x,t), \tag{18}$$

where ε is the cortical strain (i.e. change in length of cortical surface per-unit-length) and α is a proportionality constant that reflects the ability of the cortex to be compressed by ring myosin. The velocity of cortical surface movement is obtained from the following relationship (see also equation (12)).

$$v(x,t) = \int_0^x \frac{\delta\varepsilon}{\delta t}(x',t)dx'. \tag{19}$$

The conservation of mass for myosin flow results in the following

$$\frac{\partial m}{\partial t}(x,t) = -\frac{\partial}{\partial x}\big(m(x,t)v(x,t)\big) = \frac{\partial}{\partial x}(m(x,t)\int_0^x \alpha m(x',t)dx'). \tag{20}$$

If we integrate equation (20) over *x* on *(-w, w)* domain we obtain

$$dM_{ring}(t)/dt = \alpha m_{rho} M_{ring}(t), \tag{21}$$

where $M_{ring}(t) \coloneqq \int_{-w}^{w} m(x,t)dx$ is the total per-unit-length amount of ring myosin engaged in compression, $2w$ is the width of the Rho zone/contractile ring where myosin is engaged and compressing cortex and $m_{rho} \coloneqq m(w,t)$ is the concentration of myosin loaded onto the cortex when it enters the rho zone. The velocity of flow of naïve cortex into the rho zone is

$$v_{flow}(t) = \alpha M_{ring}(t)/2, \tag{22}$$

The one half is included to account for the fact that flow comes in from both sides. The solution of equation (21) is

$$M_{ring}(t) = M_{0\,ring}\, e^{t/\tau}, \tag{23}$$

where we define the characteristic time of myosin accumulation, τ, as $\frac{1}{\alpha m_{rho}}$. Note that the total amount of myosin in the ring will be the amount of engaged ring myosin plus an added baseline that would include

771 any myosin not involved in compression (see equation **Error! Reference source not found.**). We
772 assume the per-unit-length rate of ring shrinkage is proportional to the amount of ring myosin, as
773 observed in our data,

$$\frac{1}{R}\frac{dR}{dt} = -\beta M_{ring}(t), \tag{24}$$

774 where β is a proportionality coefficient that reflects the ability of the ring to be constricted by ring myosin.
775 Using equations (23) and (24), we obtain the dynamics of contractile ring size over time

$$\bar{R}(t) = \bar{R}_{ini} e^{-\beta\tau M_{0\,ring} \exp(t/\tau)}, \tag{25}$$

776 where $\bar{R}_{ini}$ is the dimensionless characteristic size of the ring; essentially the radius at minus infinity if the
777 same exponential process controlling contractile ring assembly extended back in time infinitely. Instead,
778 *in vivo* cytokinesis initiates when spindle-based signaling activates RhoA on the equatorial cortex leading
779 to the abrupt recruitment of contractile ring components. If the time frame of reference is chosen so that
780 $t = 0$ is cytokinesis onset immediately following the initial patterning of the cortex by RhoA, $M_{0\,ring}$ is the
781 amount of ring myosin immediately following this event and the initial size of the ring is

$$\bar{R}_0(t) = \bar{R}_{ini} e^{-\beta\tau M_{0\,ring}}. \tag{26}$$

782 To facilitate future use of our model for analysis of contractile ring closure data, we use the time frame of
783 reference where $t = 0$ is the point of 50% closure (i.e. $\bar{R}(t = 0) = \frac{1}{2}$), an easily identifiable time point that
784 does not rely on exact assessment of the precise onset of cytokinesis. In this reference, $M_{0\,ring} = \frac{\ln(\bar{R}_{ini})}{\beta\tau}$,
785 and by defining dimensionless velocity as $\bar{v} := \tau v$, we obtain equations (4-8). Note that equation (4) can
786 be rewritten in the following way

$$\bar{R}(\bar{t}) = \bar{R}_{ini} e^{-\frac{1}{\bar{R}}\frac{d\bar{R}}{d\bar{t}}}, \tag{27}$$

787 where $\bar{t} := t/\tau$. This relationship implies that in this dimensionless time, where $\bar{R}(\bar{t} = 0) = \frac{1}{2}$, any two
788 rings of the same size have the same dimensionless constriction rate.
789
790 ***Data availability***

All data is available from the authors upon request.

Code availability

The custom computer code used in this study is freely available from:

https://github.com/renatkh/cytokinesis.

ACKNOWLEDGEMENTS

This work was supported by a fellowship from the Jane Coffin Childs Memorial Fund to R.N.K. and grants to M.W.B from AFOSR (FA9550-08-1-0284) and the Beckman Laser Institute Foundation. J.S.G-C was supported by the University of California, San Diego Cancer Cell Biology Training Program (T32 CA067754). A.D. and K.O. receive salary and other support from the Ludwig Institute for Cancer Research. We would also like to thank Michael Glotzer for discussions that helped us align our model with current thinking about the Rho zone.

REFERENCES

Bement, W.M., H.A. Benink, and G. von Dassow. 2005. A microtubule-dependent zone of active RhoA during cleavage plane specification. *J Cell Biol*. 170:91-101.

Bement, W.M., A.L. Miller, and G. von Dassow. 2006. Rho GTPase activity zones and transient contractile arrays. *Bioessays*. 28:983-993.

Biron, D., P. Libros, D. Sagi, D. Mirelman, and E. Moses. 2004. Biphasic cytokinesis and cooperative single cell re-production. *In* Forces, Growth and Form in Soft Condensed Matter: At the Interface between Physics and Biology. A.T. Skejeltorp and A.V. Belushkin, editors. Springer, Berlin. 217-234.

Bluemink, J.G., and S.W. de Laat. 1973. New membrane formation during cytokinesis in normal and cytochalasin B-treated eggs of Xenopus laevis. I. Electron microscope observations. *J Cell Biol*. 59:89-108.

Botvinick, E.L., and M.W. Berns. 2005. Internet-based robotic laser scissors and tweezers microscopy. *Microsc Res Tech*. 68:65-74.

Bourdages, K.G., B. Lacroix, J.F. Dorn, C.P. Descovich, and A.S. Maddox. 2014. Quantitative analysis of cytokinesis in situ during C. elegans postembryonic development. *PLoS One*. 9:e110689.

Bridges, A.A., and A.S. Gladfelter. 2015. Septin Form and Function at the Cell Cortex. *J Biol Chem*. 290:17173-17180.

Byers, T.J., and P.B. Armstrong. 1986. Membrane protein redistribution during Xenopus first cleavage. *J Cell Biol*. 102:2176-2184.

Calvert, M.E., G.D. Wright, F.Y. Leong, K.H. Chiam, Y. Chen, G. Jedd, and M.K. Balasubramanian. 2011. Myosin concentration underlies cell size-dependent scalability of actomyosin ring constriction. *J Cell Biol*. 195:799-813.

Canman, J.C., D.B. Hoffman, and E.D. Salmon. 2000. The role of pre- and post-anaphase microtubules in the cytokinesis phase of the cell cycle. *Curr Biol*. 10:611-614.

Cao, L.G., and Y.L. Wang. 1990. Mechanism of the formation of contractile ring in dividing cultured animal cells. II. Cortical movement of microinjected actin filaments. *J Cell Biol*. 111:1905-1911.

Carvalho, A., A. Desai, and K. Oegema. 2009. Structural memory in the contractile ring makes the duration of cytokinesis independent of cell size. *Cell*. 137:926-937.

Carvalho, A., S.K. Olson, E. Gutierrez, K. Zhang, L.B. Noble, E. Zanin, A. Desai, A. Groisman, and K. Oegema. 2011. Acute drug treatment in the early C. elegans embryo. *PLoS One*. 6:e24656.

Chaudhuri, O., S.H. Parekh, and D.A. Fletcher. 2007. Reversible stress softening of actin networks. *Nature*. 445:295-298.

Chen, W., M. Foss, K.F. Tseng, and D. Zhang. 2008. Redundant mechanisms recruit actin into the contractile ring in silkworm spermatocytes. *PLoS Biol*. 6:e209.

D'Avino, P.P. 2009. How to scaffold the contractile ring for a safe cytokinesis - lessons from Anillin-related proteins. *J Cell Sci*. 122:1071-1079.

Dan, K. 1954. The cortical movement in Arbacia Punctulata eggs through cleavage cycles. *Embryologia*. 2:115-122.

Dan, K., and J.C. Dan. 1940. Behavior of the Cell Surface during Cleavage: III. On the formation of New Surface in the Eggs of Strongylocentrotus Pulcherrimus. *Biological Bulletin*. 78:486-501.

Dan, K., J.C. Dan, and T. Yanagita. 1938. Behaviour of the Cell Surface During Cleavage. II. *Cytologia*. 8:521-531.

Dan, K., and T. Ono. 1954. A method of computation of the surface area of the cell. *Embryologia*. 2:87-98.

Dan, K., T. Yanagita, and M. Sugiyama. 1937. Behavior of the cell surface during cleavage. I. *Protoplasma*. 28:68-81.

Danilchik, M.V., S.D. Bedrick, E.E. Brown, and K. Ray. 2003. Furrow microtubules and localized exocytosis in cleaving Xenopus laevis embryos. *J Cell Sci*. 116:273-283.

Davies, T., S.N. Jordan, V. Chand, J.A. Sees, K. Laband, A.X. Carvalho, M. Shirasu-Hiza, D.R. Kovar, J. Dumont, and J.C. Canman. 2014. High-resolution temporal analysis reveals a functional timeline for the molecular regulation of cytokinesis. *Dev Cell*. 30:209-223.

856 DeBiasio, R.L., G.M. LaRocca, P.L. Post, and D.L. Taylor. 1996. Myosin II transport, organization, and
857 phosphorylation: evidence for cortical flow/solation-contraction coupling during cytokinesis and
858 cell locomotion. *Mol Biol Cell*. 7:1259-1282.
859 Dickinson, D.J., J.D. Ward, D.J. Reiner, and B. Goldstein. 2013. Engineering the Caenorhabditis elegans
860 genome using Cas9-triggered homologous recombination. *Nat Methods*. 10:1028-1034.
861 Edelstein, A.D., M.A. Tsuchida, N. Amodaj, H. Pinkard, R.D. Vale, and N. Stuurman. 2014. Advanced
862 methods of microscope control using muManager software. *J Biol Methods*. 1.
863 Essex, A., A. Dammermann, L. Lewellyn, K. Oegema, and A. Desai. 2009. Systematic analysis in
864 Caenorhabditis elegans reveals that the spindle checkpoint is composed of two largely
865 independent branches. *Mol Biol Cell*. 20:1252-1267.
866 Farnebäck, G. 2003. Two-frame motion estimation based on polynomial expansion lecture notes in
867 computer science. Springer Science and Buisness Media. 363-370.
868 Fededa, J.P., and D.W. Gerlich. 2012. Molecular control of animal cell cytokinesis. *Nat Cell Biol*. 14:440-
869 447.
870 Fishkind, D.J., J.D. Silverman, and Y.L. Wang. 1996. Function of spindle microtubules in directing
871 cortical movement and actin filament organization in dividing cultured cells. *J Cell Sci*. 109 (Pt
872 8):2041-2051.
873 Foe, V.E., and G. von Dassow. 2008. Stable and dynamic microtubules coordinately shape the myosin
874 activation zone during cytokinetic furrow formation. *J Cell Biol*. 183:457-470.
875 Frokjaer-Jensen, C., M.W. Davis, C.E. Hopkins, B.J. Newman, J.M. Thummel, S.P. Olesen, M. Grunnet,
876 and E.M. Jorgensen. 2008. Single-copy insertion of transgenes in Caenorhabditis elegans. *Nat*
877 *Genet*. 40:1375-1383.
878 Green, R.A., E. Paluch, and K. Oegema. 2012. Cytokinesis in animal cells. *Annu Rev Cell Dev Biol*.
879 28:29-58.
880 Greenspan, H.P. 1978. On fluid-mechanical simulations of cell division and movement. *J Theor Biol*.
881 70:125-134.
882 Gudejko, H.F., L.M. Alford, and D.R. Burgess. 2012. Polar expansion during cytokinesis. *Cytoskeleton*
883 *(Hoboken)*. 69:1000-1009.
884 Hickson, G.R., A. Echard, and P.H. O'Farrell. 2006. Rho-kinase controls cell shape changes during
885 cytokinesis. *Curr Biol*. 16:359-370.
886 Hird, S.N., and J.G. White. 1993. Cortical and cytoplasmic flow polarity in early embryonic cells of
887 Caenorhabditis elegans. *J Cell Biol*. 121:1343-1355.
888 Jenkins, N., J.R. Saam, and S.E. Mango. 2006. CYK-4/GAP provides a localized cue to initiate
889 anteroposterior polarity upon fertilization. *Science*. 313:1298-1301.
890 Jordan, S.N., and J.C. Canman. 2012. Rho GTPases in animal cell cytokinesis: an occupation by the one
891 percent. *Cytoskeleton (Hoboken)*. 69:919-930.
892 Ma, X., M. Kovacs, M.A. Conti, A. Wang, Y. Zhang, J.R. Sellers, and R.S. Adelstein. 2012. Nonmuscle
893 myosin II exerts tension but does not translocate actin in vertebrate cytokinesis. *Proc Natl Acad*
894 *Sci U S A*. 109:4509-4514.
895 Mabuchi, I. 1994. Cleavage furrow: timing of emergence of contractile ring actin filaments and
896 establishment of the contractile ring by filament bundling in sea urchin eggs. *J Cell Sci*. 107 (Pt
897 7):1853-1862.
898 Maddox, A.S., B. Habermann, A. Desai, and K. Oegema. 2005. Distinct roles for two C. elegans anillins
899 in the gonad and early embryo. *Development*. 132:2837-2848.
900 Maddox, A.S., L. Lewellyn, A. Desai, and K. Oegema. 2007. Anillin and the septins promote asymmetric
901 ingression of the cytokinetic furrow. *Dev Cell*. 12:827-835.
902 Mandato, C.A., and W.M. Bement. 2003. Actomyosin transports microtubules and microtubules control
903 actomyosin recruitment during Xenopus oocyte wound healing. *Curr Biol*. 13:1096-1105.
904 Mangal, S., J. Sacher, T. Kim, D.S. Osorio, F. Motegi, A.X. Carvalho, K. Oegema, and E. Zanin. 2018.
905 TPXL-1 activates Aurora A to clear contractile ring components from the polar cortex during
906 cytokinesis. *J Cell Biol*.
907 Martineau, S.N., P.R. Andreassen, and R.L. Margolis. 1995. Delay of HeLa cell cleavage into interphase
908 using dihydrocytochalasin B: retention of a postmitotic spindle and telophase disc correlates with
909 synchronous cleavage recovery. *J Cell Biol*. 131:191-205.

910 Matsumura, F., Y. Yamakita, and S. Yamashiro. 2011. Myosin light chain kinases and phosphatase in
911 mitosis and cytokinesis. *Arch Biochem Biophys*. 510:76-82.
912 Mayer, M., M. Depken, J.S. Bois, F. Julicher, and S.W. Grill. 2010. Anisotropies in cortical tension reveal
913 the physical basis of polarizing cortical flows. *Nature*. 467:617-621.
914 Motegi, F., and A. Sugimoto. 2006. Sequential functioning of the ECT-2 RhoGEF, RHO-1 and CDC-42
915 establishes cell polarity in Caenorhabditis elegans embryos. *Nat Cell Biol*. 8:978-985.
916 Murrell, M., P.W. Oakes, M. Lenz, and M.L. Gardel. 2015. Forcing cells into shape: the mechanics of
917 actomyosin contractility. *Nat Rev Mol Cell Biol*. 16:486-498.
918 Murthy, K., and P. Wadsworth. 2008. Dual role for microtubules in regulating cortical contractility during
919 cytokinesis. *J Cell Sci*. 121:2350-2359.
920 Naganathan, S.R., S. Furthauer, M. Nishikawa, F. Julicher, and S.W. Grill. 2014. Active torque
921 generation by the actomyosin cell cortex drives left-right symmetry breaking. *Elife*. 3:e04165.
922 Otomo, T., C. Otomo, D.R. Tomchick, M. Machius, and M.K. Rosen. 2005. Structural basis of Rho
923 GTPase-mediated activation of the formin mDia1. *Mol Cell*. 18:273-281.
924 Pelham, R.J., and F. Chang. 2002. Actin dynamics in the contractile ring during cytokinesis in fission
925 yeast. *Nature*. 419:82-86.
926 Piekny, A., M. Werner, and M. Glotzer. 2005. Cytokinesis: welcome to the Rho zone. *Trends Cell Biol*.
927 15:651-658.
928 Piekny, A.J., and A.S. Maddox. 2010. The myriad roles of Anillin during cytokinesis. *Semin Cell Dev Biol*.
929 21:881-891.
930 Reymann, A.C., F. Staniscia, A. Erzberger, G. Salbreux, and S.W. Grill. 2016. Cortical flow aligns actin
931 filaments to form a furrow. *Elife*. 5.
932 Rodrigues, N.T., S. Lekomtsev, S. Jananji, J. Kriston-Vizi, G.R. Hickson, and B. Baum. 2015.
933 Kinetochore-localized PP1-Sds22 couples chromosome segregation to polar relaxation. *Nature*.
934 524:489-492.
935 Salbreux, G., G. Charras, and E. Paluch. 2012. Actin cortex mechanics and cellular morphogenesis.
936 *Trends Cell Biol*. 22:536-545.
937 Schonegg, S., A.T. Constantinescu, C. Hoege, and A.A. Hyman. 2007. The Rho GTPase-activating
938 proteins RGA-3 and RGA-4 are required to set the initial size of PAR domains in Caenorhabditis
939 elegans one-cell embryos. *Proc Natl Acad Sci U S A*. 104:14976-14981.
940 Schonegg, S., A.A. Hyman, and W.B. Wood. 2014. Timing and mechanism of the initial cue establishing
941 handed left-right asymmetry in Caenorhabditis elegans embryos. *Genesis*. 52:572-580.
942 Schroeder, T.E. 1990. The contractile ring and furrowing in dividing cells. *Ann N Y Acad Sci*. 582:78-87.
943 Sedzinski, J., M. Biro, A. Oswald, J.Y. Tinevez, G. Salbreux, and E. Paluch. 2011. Polar actomyosin
944 contractility destabilizes the position of the cytokinetic furrow. *Nature*. 476:462-466.
945 Seidel, H.S., M. Ailion, J. Li, A. van Oudenaarden, M.V. Rockman, and L. Kruglyak. 2011. A novel
946 sperm-delivered toxin causes late-stage embryo lethality and transmission ratio distortion in C.
947 elegans. *PLoS Biol*. 9:e1001115.
948 Selman, G.G., and M.M. Perry. 1970. Ultrastructural changes in the surface layers of the newt's egg in
949 relation to the mechanism of its cleavage. *J Cell Sci*. 6:207-227.
950 Shelton, C.A., J.C. Carter, G.C. Ellis, and B. Bowerman. 1999. The nonmuscle myosin regulatory light
951 chain gene mlc-4 is required for cytokinesis, anterior-posterior polarity, and body morphology
952 during Caenorhabditis elegans embryogenesis. *J Cell Biol*. 146:439-451.
953 Straight, A.F., A. Cheung, J. Limouze, I. Chen, N.J. Westwood, J.R. Sellers, and T.J. Mitchison. 2003.
954 Dissecting temporal and spatial control of cytokinesis with a myosin II Inhibitor. *Science*.
955 299:1743-1747.
956 Swann, M.M., and J.M. Mitchison. 1958. Cleavage in animal cells. *Biological Reviews*. 33:103-135.
957 Taber, L.A. 1995. Biomechanics of growth, remodeling, and morphogenesis. *Appl Mech Rev*. 48:487-
958 545.
959 Tse, Y.C., M. Werner, K.M. Longhini, J.C. Labbe, B. Goldstein, and M. Glotzer. 2012. RhoA activation
960 during polarization and cytokinesis of the early Caenorhabditis elegans embryo is differentially
961 dependent on NOP-1 and CYK-4. *Mol Biol Cell*. 23:4020-4031.
962 Tseng, Y., and D. Wirtz. 2004. Dendritic branching and homogenization of actin networks mediated by
963 arp2/3 complex. *Phys Rev Lett*. 93:258104.

964 Turlier, H., B. Audoly, J. Prost, and J.F. Joanny. 2014. Furrow constriction in animal cell cytokinesis.
965 *Biophys J*. 106:114-123.
966 Vale, R.D., J.A. Spudich, and E.R. Griffis. 2009. Dynamics of myosin, microtubules, and Kinesin-6 at the
967 cortex during cytokinesis in Drosophila S2 cells. *J Cell Biol*. 186:727-738.
968 Vavylonis, D., J.Q. Wu, S. Hao, B. O'Shaughnessy, and T.D. Pollard. 2008. Assembly mechanism of the
969 contractile ring for cytokinesis by fission yeast. *Science*. 319:97-100.
970 von Dassow, G. 2009. Concurrent cues for cytokinetic furrow induction in animal cells. *Trends Cell Biol*.
971 19:165-173.
972 Wang, Y.L., J.D. Silverman, and L.G. Cao. 1994. Single particle tracking of surface receptor movement
973 during cell division. *J Cell Biol*. 127:963-971.
974 Werner, M., E. Munro, and M. Glotzer. 2007. Astral signals spatially bias cortical myosin recruitment to
975 break symmetry and promote cytokinesis. *Curr Biol*. 17:1286-1297.
976 White, J.G., and G.G. Borisy. 1983. On the mechanisms of cytokinesis in animal cells. *J Theor Biol*.
977 101:289-316.
978 Wolpert, L. 1960. The mechanics and mechanism of cleavage. *International review of cytology*. 10:163-
979 216.
980 Wu, J.Q., V. Sirotkin, D.R. Kovar, M. Lord, C.C. Beltzner, J.R. Kuhn, and T.D. Pollard. 2006. Assembly of
981 the cytokinetic contractile ring from a broad band of nodes in fission yeast. *J Cell Biol*. 174:391-
982 402.
983 Xiong, H., W.A. Mohler, and M.C. Soto. 2011. The branched actin nucleator Arp2/3 promotes nuclear
984 migrations and cell polarity in the C. elegans zygote. *Dev Biol*. 357:356-369.
985 Yumura, S. 2001. Myosin II dynamics and cortical flow during contractile ring formation in Dictyostelium
986 cells. *J Cell Biol*. 154:137-146.
987 Zanin, E., A. Desai, I. Poser, Y. Toyoda, C. Andree, C. Moebius, M. Bickle, B. Conradt, A. Piekny, and K.
988 Oegema. 2013. A conserved RhoGAP limits M phase contractility and coordinates with
989 microtubule asters to confine RhoA during cytokinesis. *Dev Cell*. 26:496-510.
990 Zhou, M., and Y.L. Wang. 2008. Distinct pathways for the early recruitment of myosin II and actin to the
991 cytokinetic furrow. *Mol Biol Cell*. 19:318-326.
992 Zhu, Z., Y. Chai, Y. Jiang, W. Li, H. Hu, W. Li, J.W. Wu, Z.X. Wang, S. Huang, and G. Ou. 2016.
993 Functional Coordination of WAVE and WASP in C. elegans Neuroblast Migration. *Dev Cell*.
994 39:224-238.
995 Zinemanas, D., and A. Nir. 1987. Fluid mechanical simulations of cell furrowing due to anisotropic
996 surface forces. *In* Biomechanics of cell division. N. Akkas, editor. Plenum Press, New York. 281-
997 305.
998 Zinemanas, D., and A. Nir. 1988. On the viscous deformation of biological cells under anisotropic surface
999 tension. *J Fluid Mech*. 193:217-241.
000 Zumdieck, A., K. Kruse, H. Bringmann, A.A. Hyman, and F. Julicher. 2007. Stress generation and
001 filament turnover during actin ring constriction. *PLoS One*. 2:e696.

002

003

004 **FIGURES AND FIGURE LEGENDS**

Figure 1

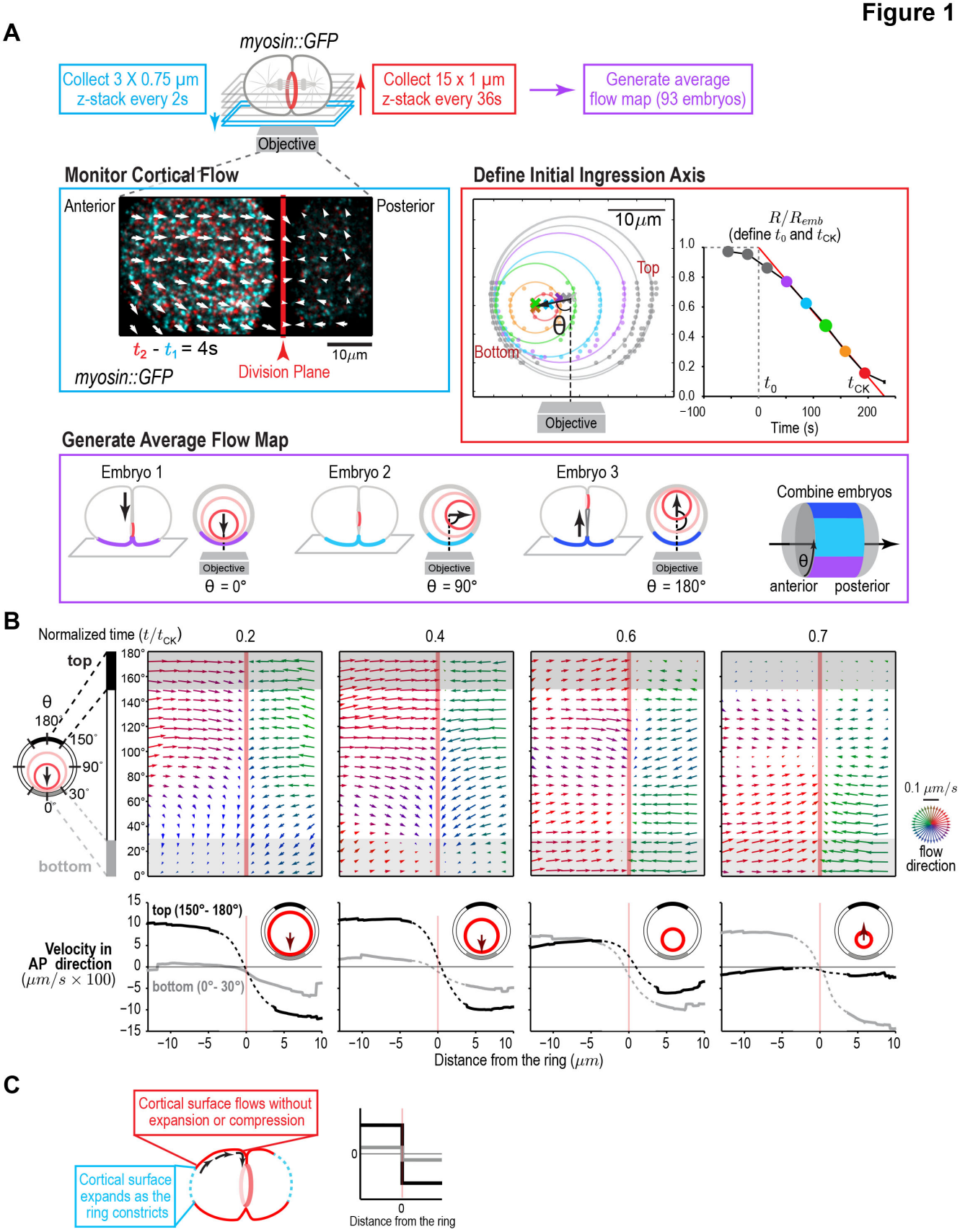

005

006 **Figure 1**. **A quantitative map of cortical surface dynamics during the first cytokinesis in the *C.***
007 ***elegans* embryo reveals that the cortical surface at the cell poles expands as the ring constricts**.
008 (**A**) (*top*) Schematic of the experimental procedure. (*middle, left*) Superposition of images of the cortex
009 acquired 4s apart. Arrows indicate cortical flow (magnified 2.5X). (*middle, right*) The initial ingression
010 axis, t_0, and t_{CK} were defined as shown for a representative embryo. The angle θ specifies the position of
011 the imaged cortex relative to the initial ingression axis. Image and quantification are representative of the
012 93 imaged embryos. (*bottom*) Angular position was used to combine data from 93 embryos to generate
013 an average flow map. (**B**) (*top*) Average flow at the indicated timepoints. Arrows show direction and
014 magnitude of the displacement in 1s (magnified 20X). (*middle*) Graphs are average velocity in the A-P
015 direction versus position along the A-P axis for the cortex on the top (*black*) and bottom (*grey*) of the
016 embryo (*shaded in flow maps*). Surface movement changes direction across the division plane, the
017 apparent velocity gradient close to the division plane is a projection artifact due to the fact that the
018 cortical surface turns inwards as it approaches the furrow from either side (dotted regions on velocity
019 curves). (**C**) Schematics show the predicted cortical velocity profile along the AP axis if surface is gained
020 at the poles; velocity would be constant in magnitude within the flow map region with opposite directions
021 on the two sides of the ring, as is experimentally observed.
022

Figure 1—figure supplement 1

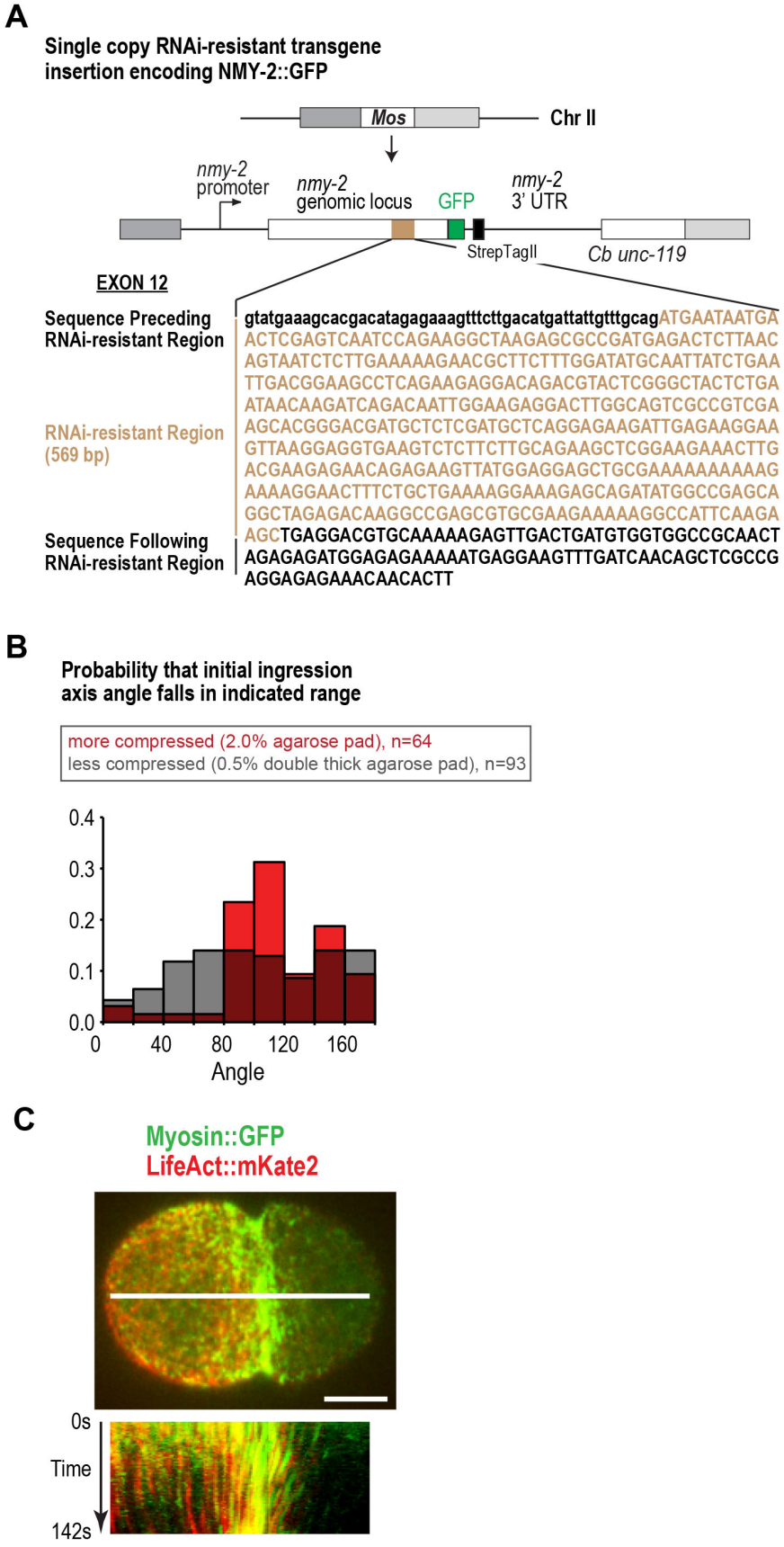

Figure 1 – Figure Supplement 1. Actin and myosin move together with the cortical surface during cytokinesis. (**A**) Schematic of the single-copy *nmy-2::gfp* transgene inserted into a specific locus on chromosome II. Cb *unc-119*, the *unc-119* coding region from the related nematode *C. briggsae*, was used as a transformation marker. The transgene was re-encoded while maintaining amino acid sequence in the indicated region to render it resistant to RNAi targeting the endogenous gene for other experiments, this feature was not used in the experiments in this manuscript. (**B**) Compression biases the direction of contractile ring closure. Graph plotting the probability that the angle between the objective axis and the initial ingression axis falls in the indicated range for embryos mounted with more (*red*) or less (*grey*) compression. Due to this bias, embryos were mounted using the low compression conditions shown in grey. (**C**) Actin and myosin move together with the cortical surface during cytokinesis. The white line in the center of the image (*top*) indicates the region used for the kymograph (*bottom*). Image is representative of 5 imaged embryos. Scale bar is 10μm.

Figure 1—figure supplement 2

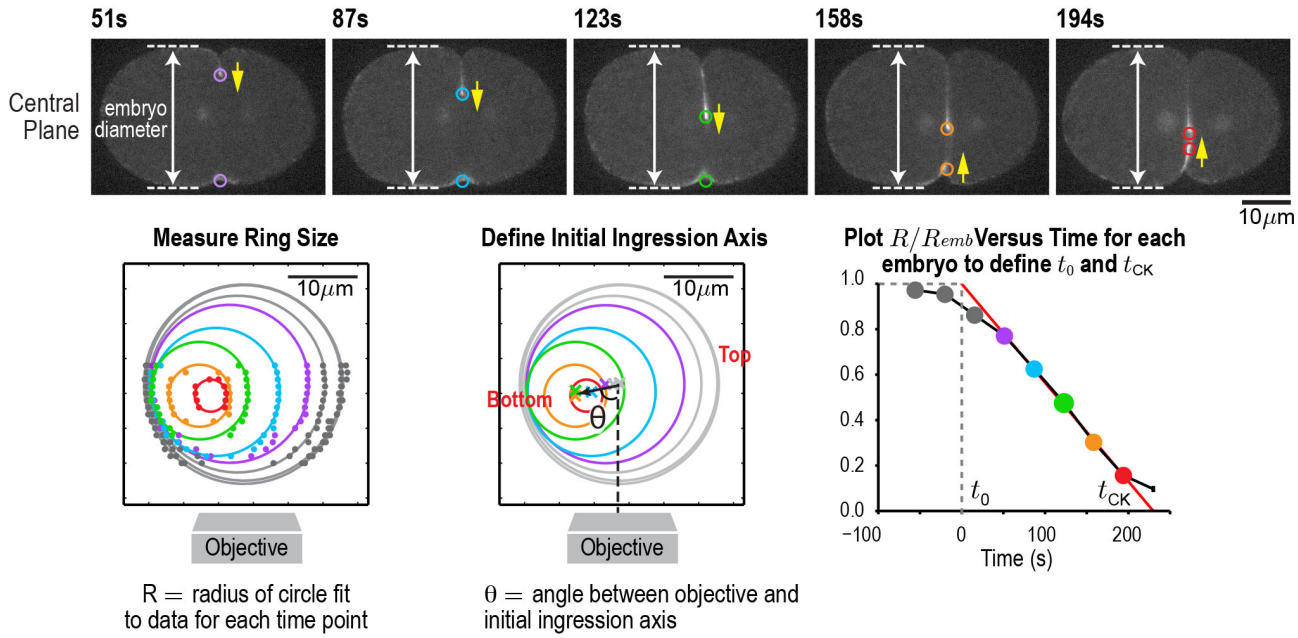

Figure 1 – Figure Supplement 2. An automated method for monitoring contractile ring closure. (*top*) Central plane images of the embryo in Figure 1A. Panels on the lower left and lower right are reproduced from Figure 1A for comparison. An automated algorithm was used to identify the edges of the embryo (dashed lines) and the position of the contractile ring (colored circles) in each z-plane. Yellow arrows mark the direction of furrow ingression and illustrate how the furrow initially ingresses from the top and then changes directions to ingress from the bottom during the second half of cytokinesis. (*lower left*) Points marking contractile ring position in the z-planes were projected onto an end-on view of the division plane. Data for different timepoints in this representative embryo are shown in colors corresponding to the circles in the central plane images. Ring sizes were measured by fitting circles to the data. (*middle*) The initial axis of contractile ring closure was defined by the angle θ between the objective axis and a line fit through the centers of the contractile rings with a normalized size > 0.3. (*right*) = A plot of normalized ring size versus time for this embryo defines t_0 and t_{CK} as the times when a line fit through the points corresponding to ring sizes between 0.3 and 0.8 crossed 1 and 0, respectively. Scale bar is 10μm.

Figure 1—figure supplement 3

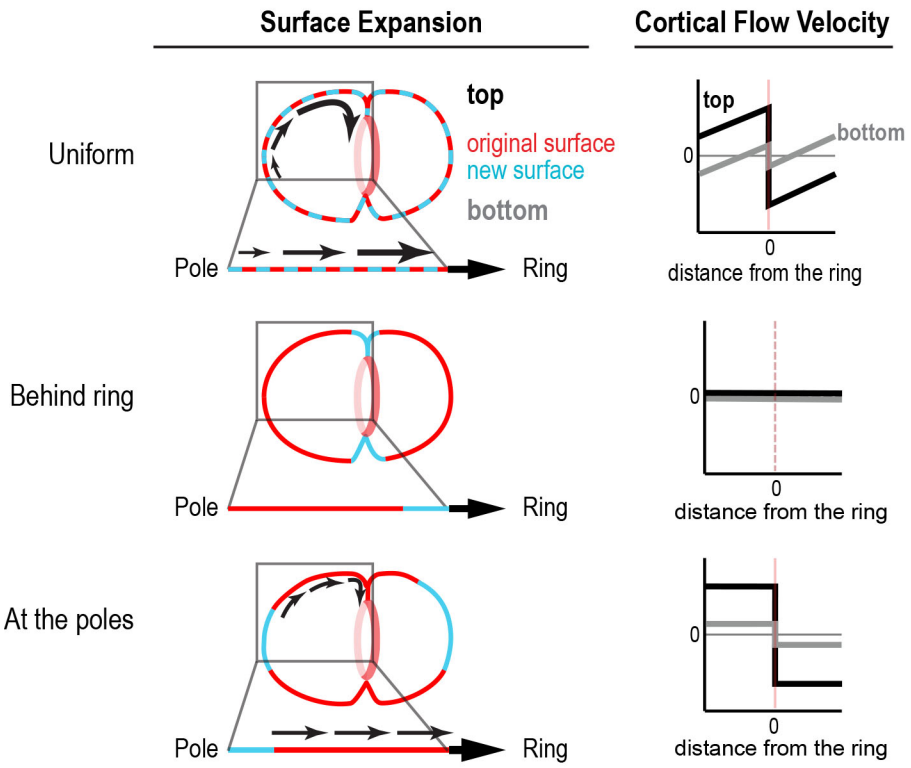

Figure 1 – Figure Supplement 3. Different profiles of cortical surface velocity along the A-P axis are predicted for different spatial patterns of surface gain. (*top*) For surface gain behind the ring, no cortical movement is predicted on the embryo surface. (*middle*) For uniform surface gain, a gradient of velocities will be observed, where the cortex immediately behind the ring moves at the speed of the ingressing furrow, and cortical velocity decreases linearly towards the cell poles. (*bottom*) Reproduced from Figure 1C for comparison. If surface is gained only at the poles, cortical velocity will be constant in magnitude within the flow map region with opposite direction on the two sides of the ring.

Figure 2

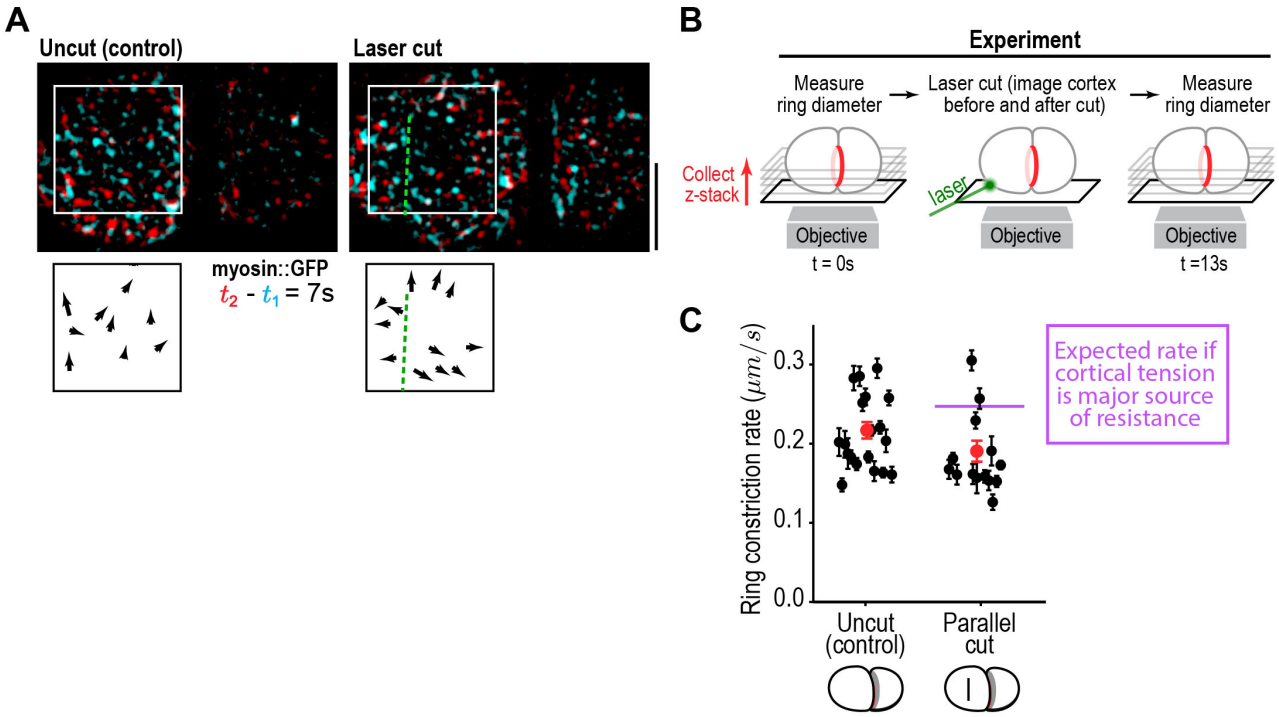

Figure 2. Cortical tension does not limit the rate of ring closure. (**A**) The success of cortical cuts was assessed by comparing surface images of cortical myosin before (*cyan*) and after (*red*) the cut to monitor the movement of myosin foci away from the cut site. Representative images are shown. Scale bar is 10 µm. (**B**) Schematic of laser ablation experiment to determine if cortical resistance limits the rate of contractile ring closure. Contractile ring sizes were measured from z-stacks acquired before and 13s after a cut was made across the cortex with a laser. (**C**) Graph plots the rates of ring closure derived from before and after ring size measurements for uncut controls (n=19 embryos) and embryos with cuts parallel to the division plane (n=14 embryos). Black symbols are single embryo measurements with measurement errors. Red symbols are the means; error bars are the SEM. The purple line marks expected closure rate if cortical tension is a major source of resistance.

097

Figure 2—figure supplement 1

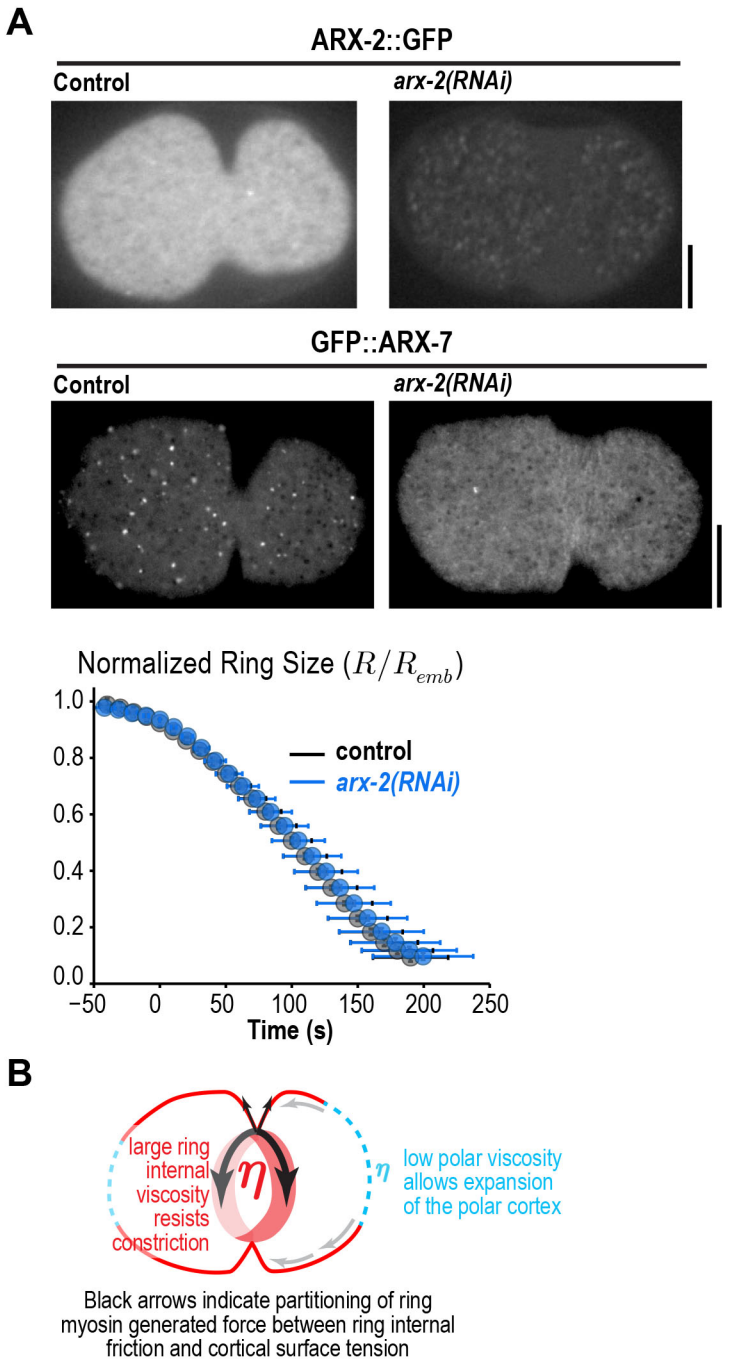

Figure 2 – Figure Supplement 1. Arp2/3 depletion does not alter ring constriction kinetics. (**A**) Images of cortical ARX-2::GFP (*top*) and GFP::ARX-7 (*middle*) in control and *arx-2(RNAi)* embryos confirm loss of cortical Arp2/3 complex (images are representative of 10 imaged embryos for each condition in the GFP::ARX-7 strain and 15 for control and 13 for *arx-2(RNAi)* in the ARX-2::GFP strain). Scale bars are 10µm. (*bottom*) Graph plots average contractile ring size versus time for control (*grey*) and *arx-2(RNAi)* (*blue*) embryos expressing myosin::GFP (n= 93 embryos for control and 68 embryos for *arx-2(RNAi)*). Error bars are standard deviation. (**B**) Schematic illustrating the partitioning of ring myosin generated force between ring internal friction and cortical surface tension. Ring myosin generated force primarily counters ring internal friction to drive constriction. The low viscosity of the polar cortex causes it to expand when it comes under tension due to the constricting ring.

126

Figure 3

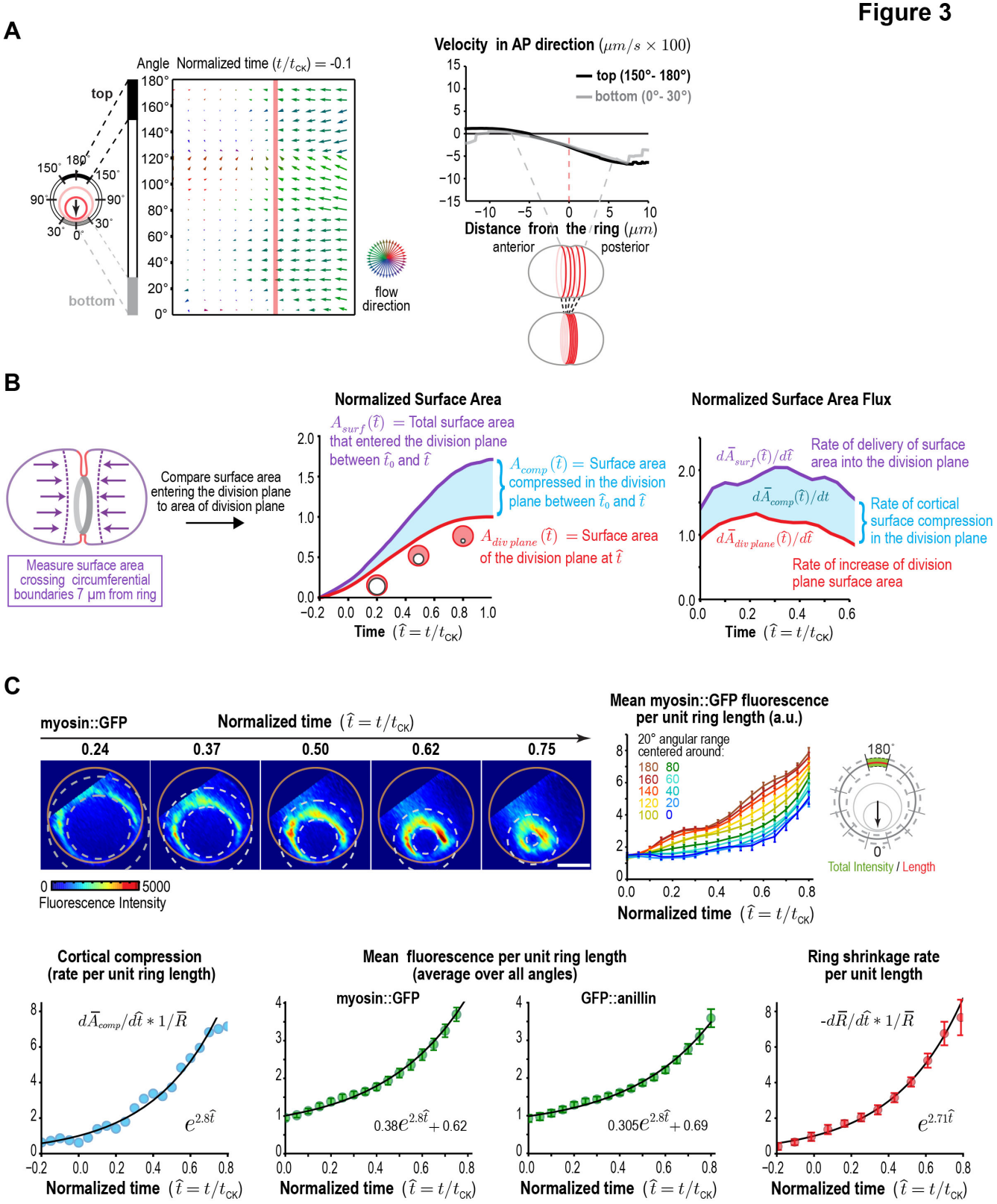
A
Angle Normalized time (t/t_{CK}) = -0.1
top
bottom
flow direction
Velocity in AP direction $(\mu m/s \times 100)$
top (150°- 180°)
bottom (0°- 30°)
Distance from the ring (μm)
anterior
posterior
B
Compare surface area entering the division plane to area of division plane
Measure surface area crossing circumferential boundaries 7 μm from ring
Normalized Surface Area
$A_{surf}(\hat{t})$ = Total surface area that entered the division plane between $\hat{t}_0$ and $\hat{t}$
$A_{comp}(\hat{t})$ = Surface area compressed in the division plane between $\hat{t}_0$ and $\hat{t}$
$A_{div\ plane}(\hat{t})$ = Surface area of the division plane at $\hat{t}$
Time $(\hat{t} = t/t_{CK})$
Normalized Surface Area Flux
$d\bar{A}_{surf}(\hat{t})/d\hat{t}$
Rate of delivery of surface area into the division plane
$d\bar{A}_{comp}(\hat{t})/dt$
Rate of cortical surface compression in the division plane
$d\bar{A}_{div\ plane}(\hat{t})/d\hat{t}$
Rate of increase of division plane surface area
Time $(\hat{t} = t/t_{CK})$
C
myosin::GFP
Normalized time $(\hat{t} = t/t_{CK})$
0.24
0.37
0.50
0.62
0.75
0
5000
Fluorescence Intensity
Mean myosin::GFP fluorescence per unit ring length (a.u.)
20° angular range centered around:
180 80
160 60
140 40
120 20
100 0
Total Intensity / Length
Normalized time $(\hat{t} = t/t_{CK})$
Cortical compression (rate per unit ring length)
$d\bar{A}_{comp}/d\hat{t} * 1/\bar{R}$
$e^{2.8\hat{t}}$
Mean fluorescence per unit ring length (average over all angles)
myosin::GFP
$0.38e^{2.8\hat{t}} + 0.62$
GFP::anillin
$0.305e^{2.8\hat{t}} + 0.69$
Ring shrinkage rate per unit length
$-d\bar{R}/d\hat{t} * 1/\bar{R}$
$e^{2.71\hat{t}}$
Normalized time $(\hat{t} = t/t_{CK})$

Figure 3. Ring myosin compresses cortical surface along the axis perpendicular to the ring, pulling in new cortical surface at a rate proportional to the amount of ring myosin. (**A**) The equatorial cortex is compressed during contractile ring assembly. Following the onset of spindle-based RhoA signaling, the initial recruitment of contractile ring proteins leads to uniform compression of cortical surface along the axis perpendicular to the forming ring across a 10 μm wide region spanning the cell equator. (*left*) Average flow map at (t/t_{CK}=-0.1) immediately after the onset of spindle-based signaling (n= 93 embryos). (*middle*) The surface velocity profile reveals a linear velocity gradient that spans the cell equator (-5 to +5 μm), indicating a zone of cortical compression. (**B**) Cortical compression within the ring continues during constriction. (*left graph*) Plot comparing the area of the forming division plane (*red*) with the total cortical surface area that entered the division plane from the start of cytokinesis (*purple*; calculated as indicated in the schematic). (*right graph*) Plot comparing the rate of delivery of cortical surface into the division plane (*purple*) with the rate of growth of the division plane (*red*). The difference between the two is the rate of cortical surface compression (*cyan*). (**C**) The per-unit-length amount of ring myosin and the rate of cortical compression increase with the same exponential kinetics. (*top left*) Representative images of the division plane in embryos expressing myosin::GFP reconstructed from 40-plane z-stacks. Gold circles mark the embryo boundary and dashed circles mark the boundaries used for ring intensity measurements. (*top right*) Graph plots per-unit-length myosin::GFP fluorescence for the indicated angular ranges (n=36 embryos). (*bottom left*) Graph plots the rate of cortical surface compression per unit ring length (n=93 embryos). (*bottom middle*) Graphs plot mean per-unit-length myosin::GFP (n=36 embryos) and GFP::anillin (n=26 embryos) fluorescence (n=36 embryos) in the ring. (*bottom right*) Graph plots the per-unit-length rate of ring closure. Black lines are fitted single exponentials. Error bars are the SEM.

Figure 3—figure supplement 1

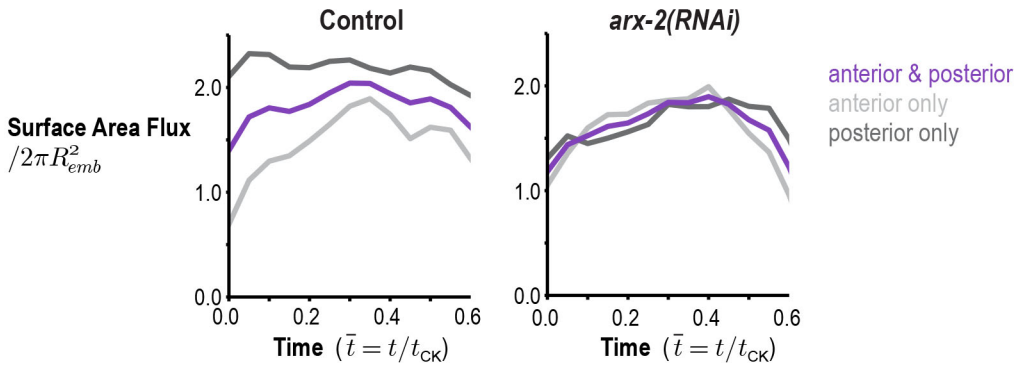

Figure 3 – Figure Supplement 1. Arp2/3 inhibition abolishes the asymmetry in the amount of cortex entering the division plane from the anterior and posterior sides. Graphs plot the rate of cortical flux across the anterior (*light grey*) and posterior (*dark grey*) boundaries (see schematic in Figure 3B) versus the mean for the two sides (*purple*) for control and *arx-2(RNAi)* embryos. Calculated from the average flow maps for the control (n= 93 embryos) and *arx-2(RNAi)* (n= 68 embryos) conditions.

Figure 3—figure supplement 2

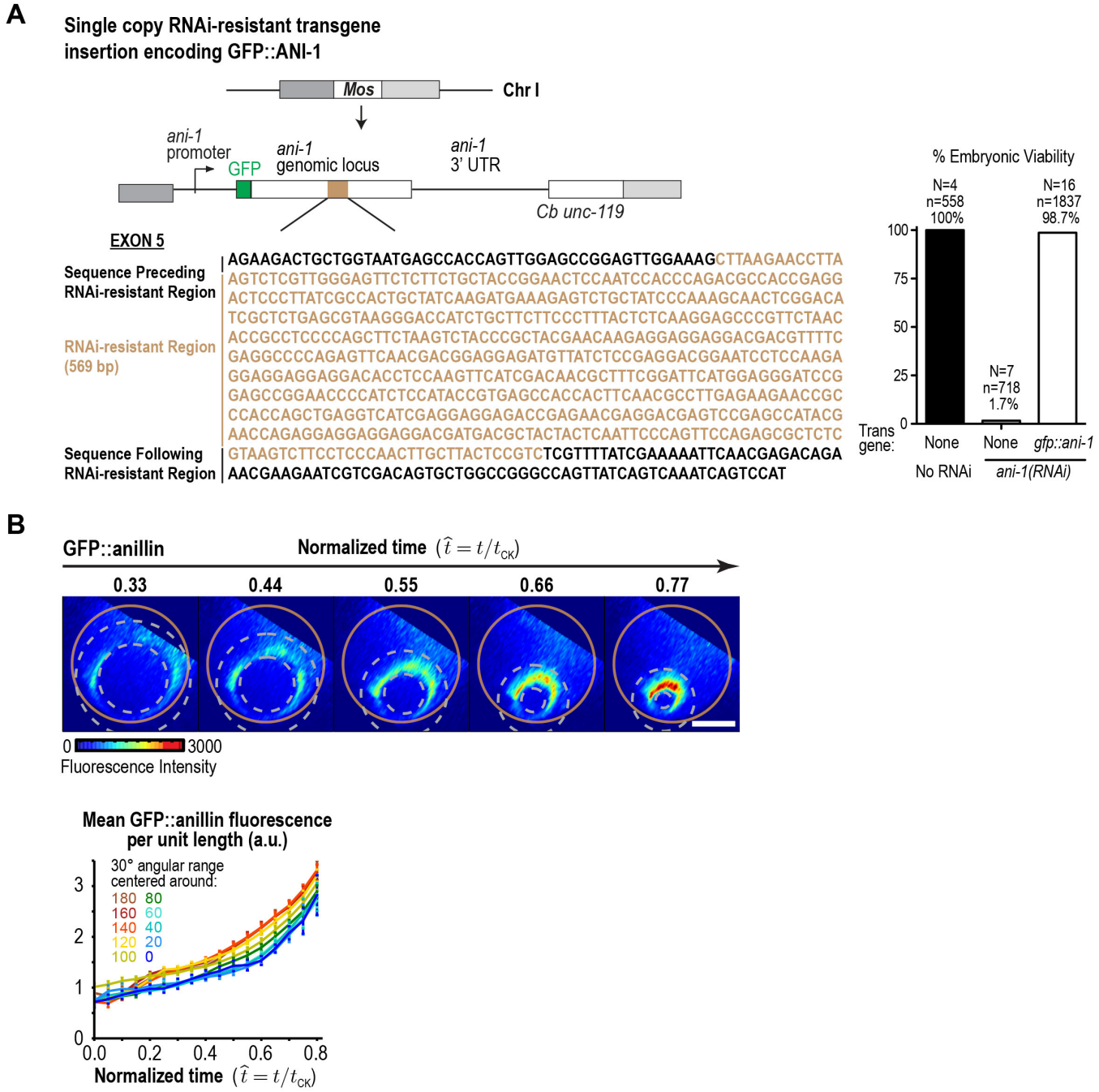

Figure 3 – Figure Supplement 2. GFP::anillin fluorescence in the ring increases exponentially during constriction. (**A**) (*left*) Schematic of the single-copy *gfp::ani-1* trangene. The transgene was re-encoded while maintaining amino acid sequence in the indicated region to render it resistant to RNAi targeting of the endogenous *ani-1* gene to allow testing of the functionality of the GFP::ANI-1 fusion. (*right*) Graph plotting embryonic lethality demonstrates that the *gfp::ani-1* transgene is functional. (**B**) (*top*) Images of the division plane in an embryo expressing GFP::anillin. (*bottom*) Graph plots GFP::anillin fluorescence per unit length of the ring for the indicated angular ranges. Error bars are the SEM.

Figure 3—figure supplement 3

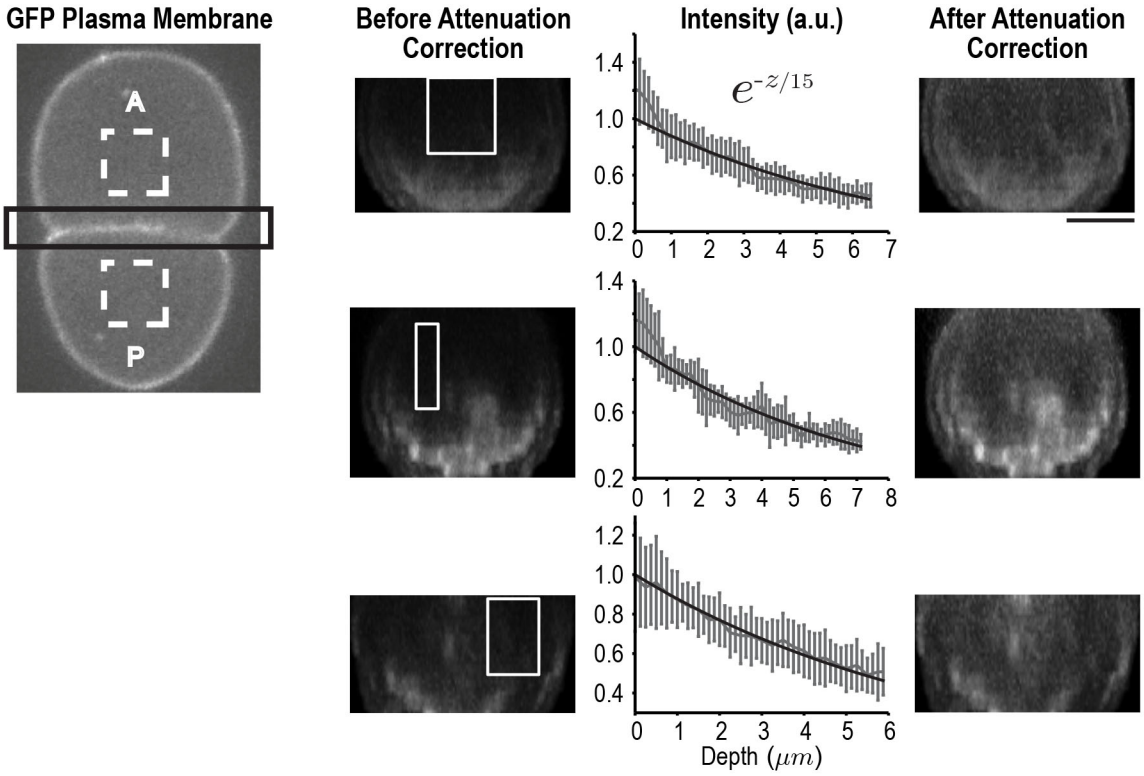

Figure 3 – Figure Supplement 3. Correcting for signal attenuation with sample depth. Fluorescence attenuation with embryo depth was estimated from fluorescence intensity measurements made at the cell-cell boundary of the 2-cell embryos expressing a GFP-tagged plasma membrane marker. Cell-cell boundaries were reconstructed from 40 plane z-stacks. The intensity profile at each slice was calculated by subtracting the average background intensity estimated from dashed rectangles (left) from the cell-cell boundary region (black rectangle) at each slice and calculating the maximum intensity projection along AP axis. The effect of depth on signal was calculated from the reconstructed division planes by plotting the mean signal as a function of depth in 10 rectangular regions (white boxes) where the signal was expected to be uniform; three examples are shown here. All intensity profiles were simultaneously fitted using a single exponential. Error bars are the SD. On the right, the same cell-cell boundaries are shown after correction for depth attenuation. The scale bar is 10 μm.

Figure 3—figure supplement 4

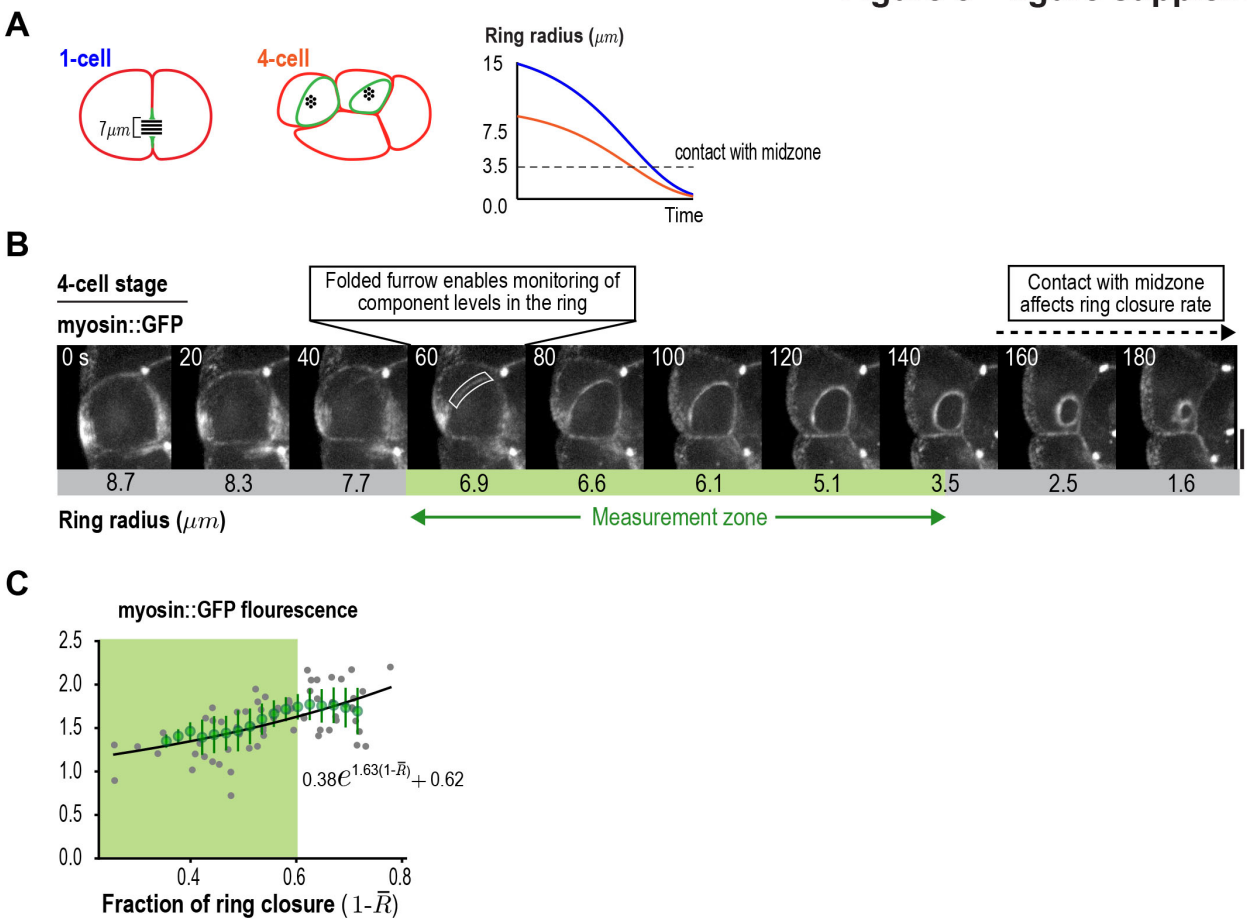

Figure 3 – Figure Supplement 4. Ring component dynamics at the 4-cell stage are consistent with exponential accumulation. (**A**). (*left*) Schematic illustrating the relative geometries of cytokinesis in 1- and 4-cell stage *C. elegans* embryos. (right) The range of ring sizes between furrow formation and contact with the midzone, which occurs at a ring radius of about 3.5 μm in all divisions and alters constriction rate and component accumulation (Carvalho et al., 2009), is much smaller at the 4-cell stage than at the 1-cell stage. (**B**) Myosin levels in the ring can only be monitored over a limited range of ring size at the 4-cell stage. Images of the division plane in a representative dividing cell at the 4-cell stage reconstructed from 16x1μm z-stacks of an embryo expressing myosin::GFP (n=16 embryos imaged). The range of ring sizes for which myosin levels can be measured is indicated (*Measurement zone*). (**C**) Graph plotting measured mean per-unit-length myosin::GFP fluorescence in the ring at the 4-cell stage fit to an exponential equation with the same baseline contribution as the 1-cell stage data in Figure 3C (*black line*). Error bars are the SEM.

Figure 4

A

Compression Feedback model

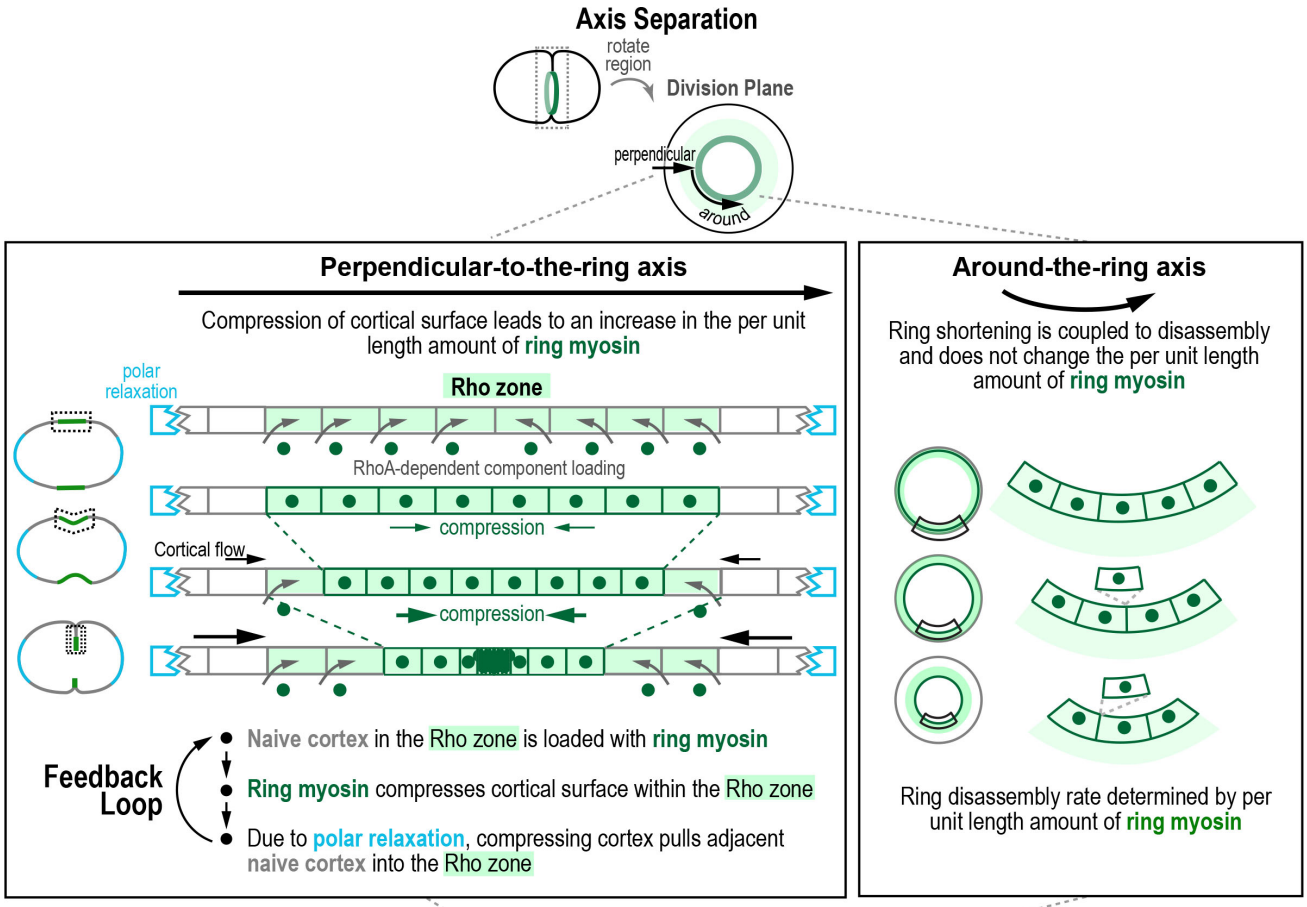

B

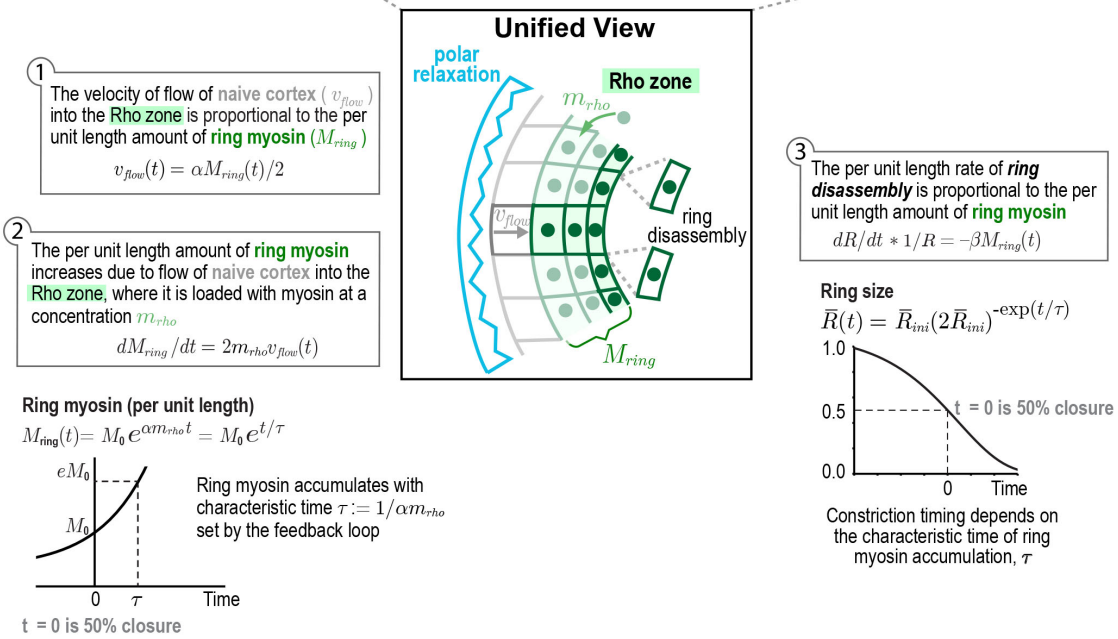

Figure 4. Compression Feedback model of cytokinesis. (**A**) The natural coordinate system for contractile ring dynamics has two axes, an axis parallel to ring constriction (*around-the-ring axis*) and an axis perpendicular to the ring (*perpendicular-to-the-ring axis*). Polar relaxation and filament alignment in the around-the-ring direction lead to anisotropy in behavior along the two axes, which are illustrated separately here. Along the axis perpendicular to the ring, feedback between ring myosin and compression-driven cortical flow leads to an exponential increase in the per-unit-length amount of ring myosin. Along the around-the-ring axis, constriction is coupled to disassembly and does not change the per-unit-length amount of ring myosin. (**B**) Formulation of the proposed mechanisms as an analytical mathematical model consisting of three equations and three model parameters. (*left*) Equations (1) and (2) describe the feedback loop between the amount of ring myosin and the velocity of compression-driven flow of cortical surface into the ring. Solving these equations gives the expression for the per-unit-length amount of ring myosin, which accumulates exponentially as shown in the graph. (*right*) The feedback loop operating perpendicular to the ring controls the per-unit-length amount of ring myosin, which in turn controls the per-unit-length rate of ring constriction as described in equation (3). Graph plots the equation for ring size resulting from solving the model equations in the time reference where $t = 0$ is the halfway point of ring closure.

Figure 5

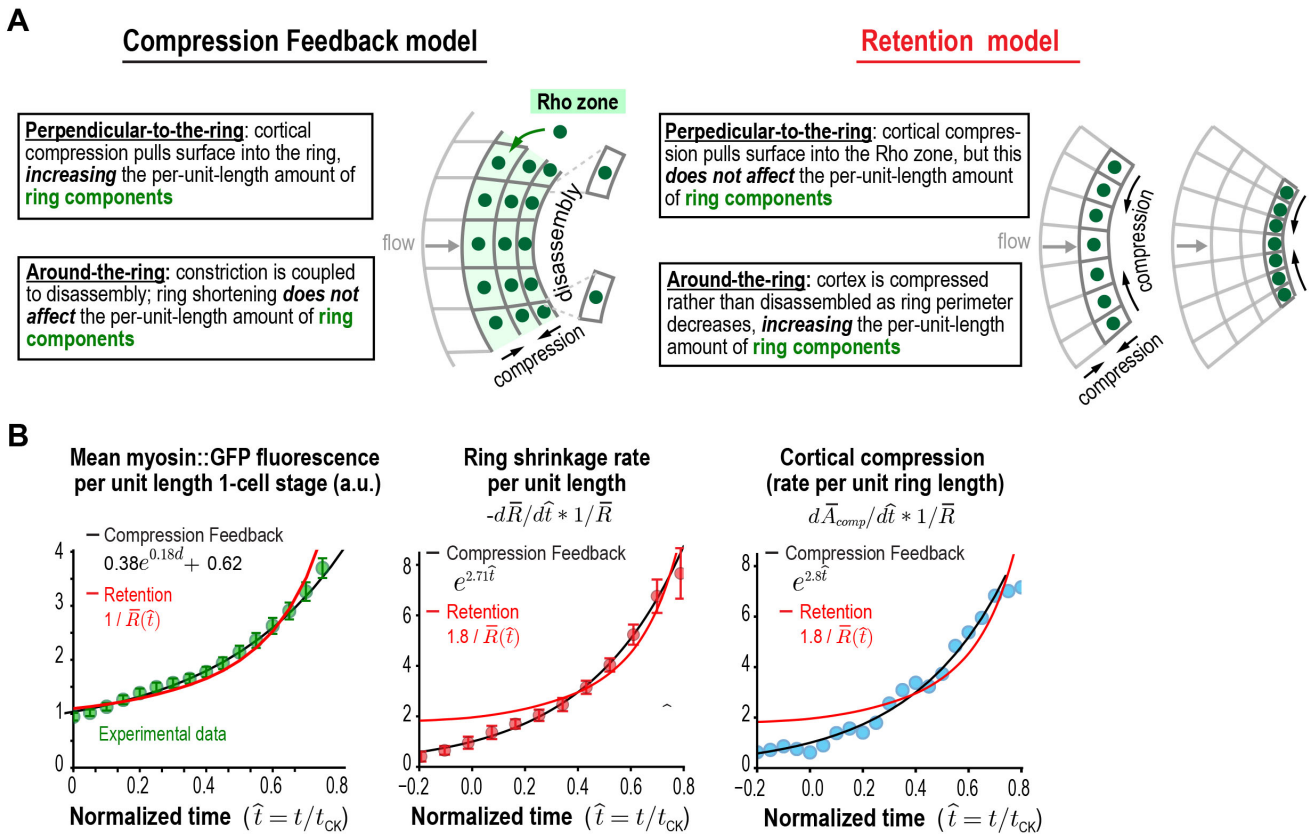

Figure 5. Myosin and anillin accumulation and the rates of ring constriction and cortical compression support the Compression Feedback model. (**A**) Two models could explain the acceleration in the per-unit-length constriction rate during constriction. In the Compression Feedback model, acceleration results from a feedback loop between ring myosin and compression-driven cortical flow in the perpendicular-to-the-ring direction. In the Retention model, compression without disassembly in the around-the-ring direction increases the per-unit-length amounts of ring components. (**B**) Graphs show mean per-unit-length myosin::GFP fluorescence in the ring along with the per-unit-length constriction and cortical compression rates. Myosin fluorescence data is reproduced from Figure 3C to allow comparison of the best fits for the Compression Feedback (*black lines*) and Retention (*red lines*) models.

Figure 5—figure supplement 1

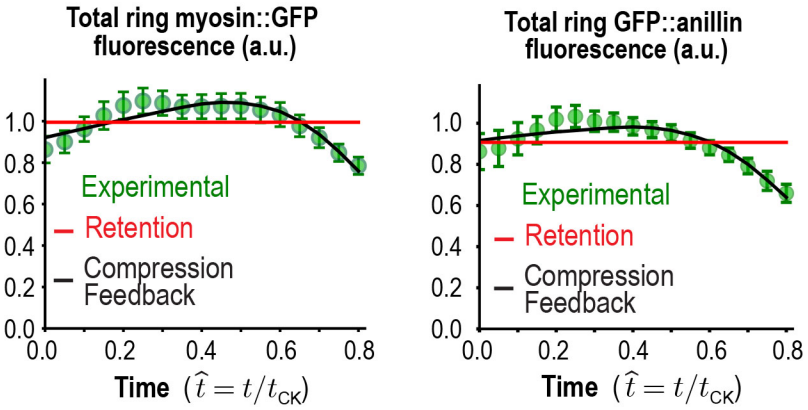

228

229 **Figure 5 – Figure Supplement 1. Total myosin::GFP and GFP::anillin in the ring.** Graphs plotting
230 mean total ring fluorescence (average over all angles; *green*) for myosin::GFP (n=36 embryos) and
231 GFP::anillin (n=26 embryos). Error bars are the SEM. The predictions for the Compression Feedback
232 (*black lines*) and Retention (*red lines*) models are also shown. Error bars are the SEM.

233

Figure 6

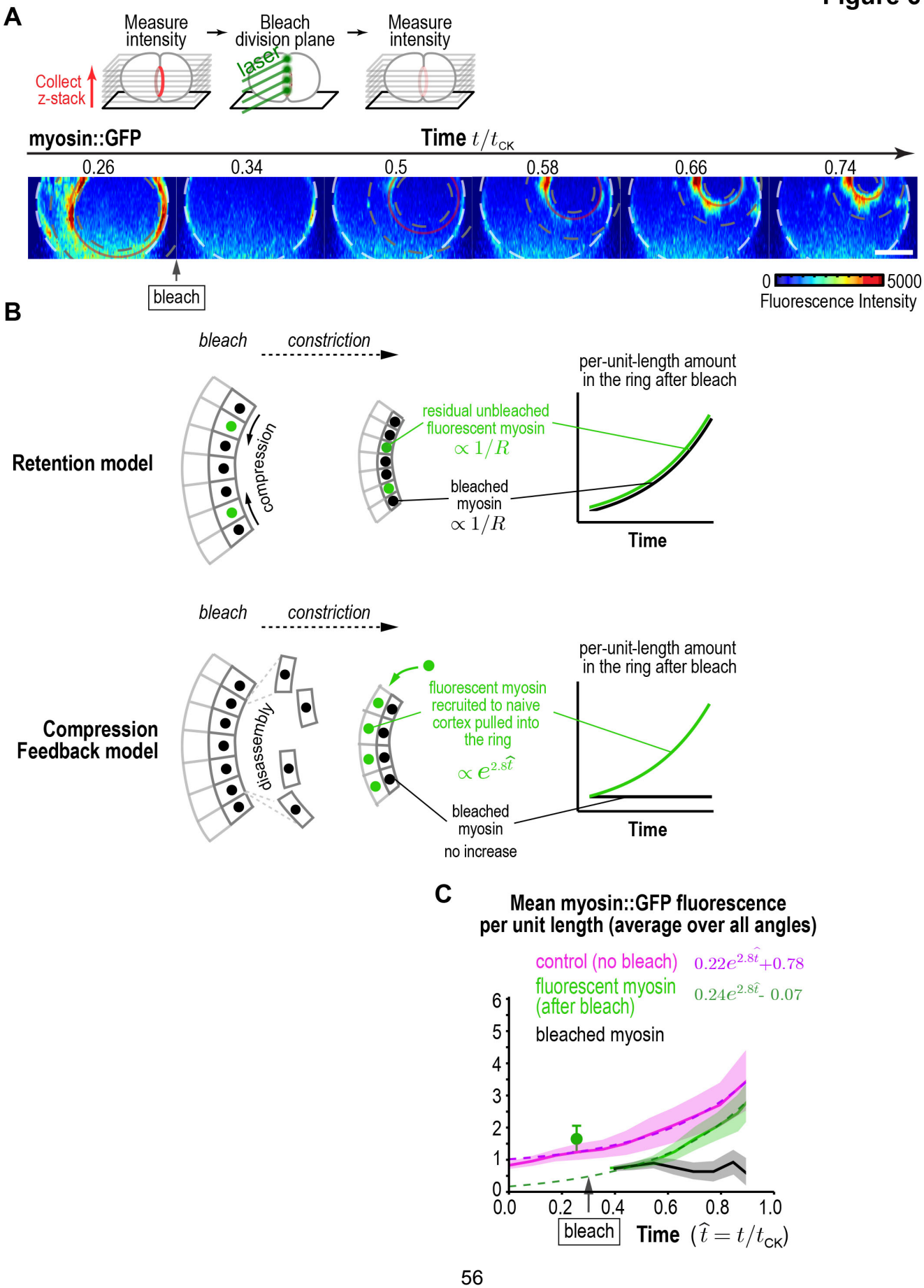
A
Measure intensity
Bleach division plane
Measure intensity
Collect z-stack
laser
myosin::GFP
Time t/t_{CK}
0.26
0.34
0.5
0.58
0.66
0.74
bleach
0
5000
Fluorescence Intensity
B
bleach
constriction
Retention model
compression
residual unbleached fluorescent myosin
$\propto 1/R$
bleached myosin
$\propto 1/R$
per-unit-length amount in the ring after bleach
Time
bleach
constriction
Compression Feedback model
disassembly
fluorescent myosin recruited to naive cortex pulled into the ring
$\propto e^{2.8\hat{t}}$
bleached myosin
no increase
per-unit-length amount in the ring after bleach
Time
C
Mean myosin::GFP fluorescence per unit length (average over all angles)
control (no bleach)
$0.22e^{2.8\hat{t}}+0.78$
fluorescent myosin (after bleach)
$0.24e^{2.8\hat{t}}-0.07$
bleached myosin
0
1
2
3
4
5
6
0.0
0.2
0.4
0.6
0.8
1.0
bleach
Time $(\hat{t} = t/t_{CK})$

234

235 **Figure 6. Fluorescence recovery after photobleaching of the division plane supports the**
236 **Compression Feedback model.** (**A**) (*top*) Schematic of the photobleaching experiment. (*bottom*)
237 Images of the division plane reconstructed from 30x1μm z-stacks of an embryo expressing myosin::GFP
238 whose division plane was bleached at t/t_{CK} ~0.3. Red circle marks the contractile ring and dashed circles
239 mark the boundaries used for ring intensity measurements. Image series is representative of 8 imaged
240 embryos. (**B**) Schematics illustrate the expected results predicted by the Retention and Compression
241 Feedback models. (**C**) Graph plotting the mean per-unit-length amounts of fluorescent myosin::GFP in
242 the ring for control embryos (*pink*, n=24 embryos) and embryos in which the division plane was bleached
243 at the indicated time (*green*, n=8 embryos). The amount of bleached myosin::GFP in the ring (*black*) was
244 calculated as the difference between the control and after bleach curves. Solid continuous lines are the
245 average curves with errors shown as shaded regions. Dashed lines are exponential fits to the data.
246 Errors for the control and after bleach data are SD and errors for the difference are SEM. Scale bar is 10
247 μm.
248

Figure 6—figure supplement 1

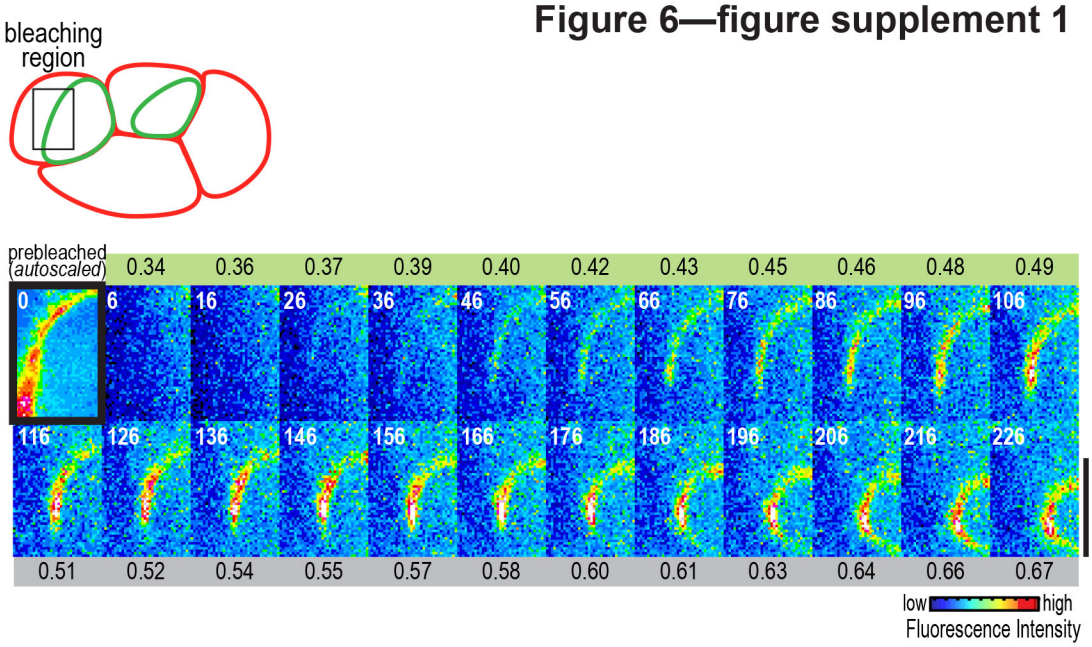

Figure 6 – Figure Supplement 1. Recovery of myosin::GFP fluorescence after division plane bleaching at the 4-cell stage. To test whether compression-driven cortical flow delivers components to the ring at the 4-cell stage as well as at the 1-cell stage, we monitored recovery after photobleaching the entire contractile arc. Images show a representative bleached embryo (n=10). The observed recovery pattern was very similar to what we observed at the 1-cell stage. Scale bar is 10 μm.

Figure 7

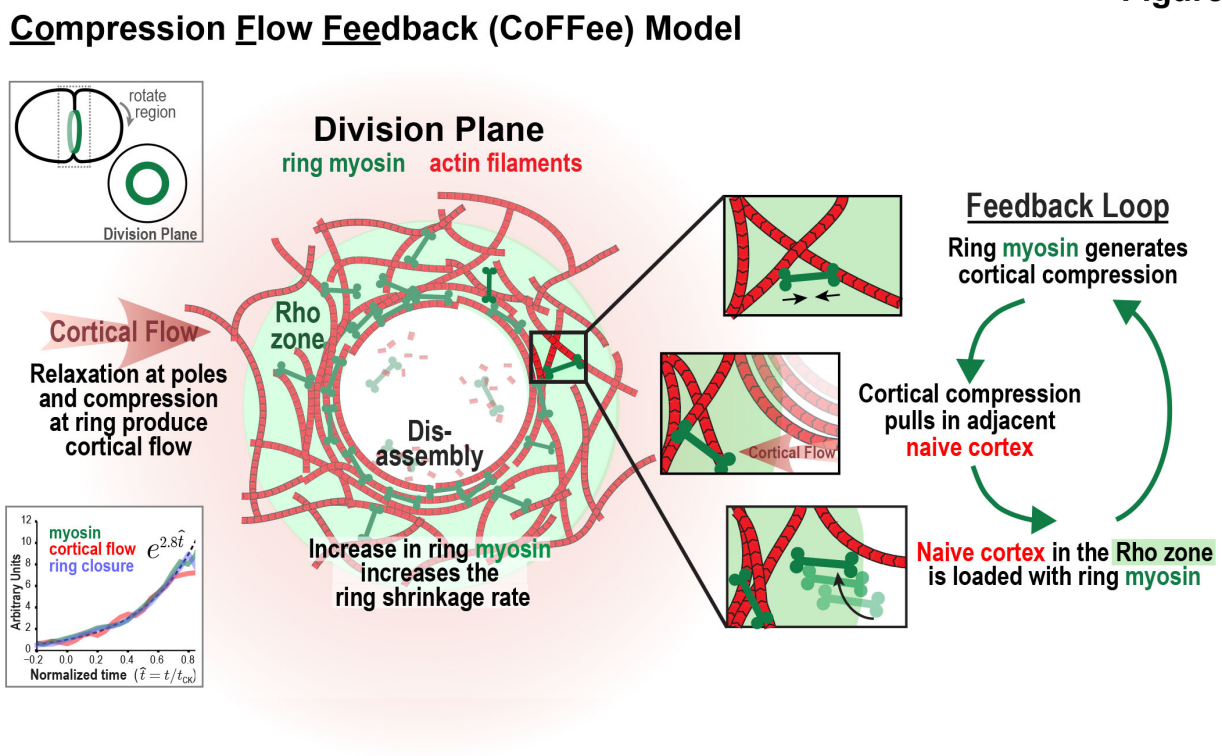

Figure 7. The Compression Feedback model: a feedback loop operating in the perpendicular-to-the-ring direction accelerates the per-unit-length constriction rate during ring closure. Schematic summary of the Compression Feedback model for cytokinesis. Polar relaxation allows ring myosin to compress cortical surface along the axis perpendicular-to-the-ring, which pulls more cortical surface that is loaded with myosin into the ring. Feedback between ring myosin and compression-driven cortical flow leads to an exponential increase in the per-unit-length amount of ring myosin that maintains the high overall closure rate as ring perimeter decreases.

SUPPLEMENTARY VIDEO LEGENDS

Video 1. Cortical flow imaged in a control embryo expressing myosin::GFP. Playback is 6x realtime. The video is constructed from maximum intensity projection of 3 x 0.75 μm plane z-stacks acquired at 2 s intervals. The red line marks the position of the division plane. The arrows represent the surface movement between consecutive frames at the base of the arrow. The length of the arrow is 5 times the magnitude of movement. The direction is also color coded according to the color wheel as shown in Figure 1B.

Video 2. Average cortical flow map calculated from time lapse imaging of the cell surface in 93 control embryos expressing myosin::GFP. (*top, left*) Schematic illustrates location of the cylindrical surface covered by the map. (*top, right*) Dynamic schematic illustrates ring size and position for each value of t/t_{CK}. (*bottom, left*) The movement of each blue dot corresponds to surface movement at its location. The y-axis is the angular position relative to the initial ingression axis. The x-axis is the distance from the division plane along the anterior-posterior axis. (*bottom, right*) Dynamic graph plots the magnitude of the component of surface velocity aligned along the anterior-posterior axis for the top (150-180°; black) and bottom (0-30°; grey) regions of the cortex.

Video 3. Average cortical flow map calculated from time lapse imaging of the cell surface in 68 *arx-2(RNAi)* embryos expressing Myosin::GFP. (*top, left*) Schematic illustrates the location of the cylindrical surface covered by the map. (*top, right*) Dynamic schematic illustrates ring size and position for each value of t/t_{ck}. (*bottom, left*) The movement of each blue dot corresponds to surface movement at its location. The y-axis is the angular position relative to the initial ingression axis. The x-axis is the distance from the division plane along the anterior-posterior axis. (*bottom, right*) Dynamic graph plots the magnitude of the component of surface velocity aligned along the anterior-posterior axis for the top (150-180°; black) and bottom (0-30°; grey) regions of the cortex.